Revision 1:

Two-stage magmatism and tungsten mineralization in the Nanling Range, South China: Evidence from the Jurassic Helukou deposit

JINGYA CAO [1], HUAN LI [2,*], THOMAS J. ALGEO [3, 4, 5], LIZHI YANG[2], LANDRY SOH TAMEHE[2]

1. CAS Key laboratory of Crust-Mantle Materials and Environments, University of Science and Technology of China, Hefei 230026, China

2. Key Laboratory of Metallogenic Prediction of Nonferrous Metals and Geological Environment Monitoring, Ministry of Education, Central South University, Changsha 410083, China

3. Faculty of Earth Resources, State Key Laboratory of Geological Processes and Mineral Resources, China University of Geosciences, Wuhan 430074, China

4. State Key Laboratory of Biogeology and Environment Geology, School of Earth Sciences, China University of Geosciences, Wuhan 430074, China

5. Department of Geology, University of Cincinnati, Cincinnati, OH 42221-0013, USA

Corresponding author: lihuan@csu.edu.cn (H. Li)

Abstract: The Helukou deposit, with proven reserves of 33,752 t WO_3, is one of the newly exploited medium-scale tungsten (W) deposits in the Guposhan ore field, Nanling Range of South China. Skarn-type and less abundant altered granite-type tungsten orebodies were identified in this deposit. The ore mineralization in this district

was a product of two-stage magmatism, as shown by LA–ICP–MS U–Pb dating of zircons and Re–Os dating of molybdenite. The former yielded U–Pb ages of 184.0 ± 3.6 Ma (MSWD = 0.15) and 163.8 ± 1.5 Ma (MSWD = 0.41) for fine-grained biotite granite and muscovite granite, respectively, as well as a U–Pb age of 181.5 ± 2.1 Ma (MSWD = 0.75) for zircon grains from altered granite-type tungsten ore. The latter yielded molybdenite Re–Os ages of 183.5 ± 2.8 Ma (without MSWD owing to a limited number of samples) and 163.4 ± 2.8 Ma (MSWD = 0.71) for altered granite-type and skarn-type tungsten deposits, respectively. Thus, two separate tungsten mineralization events occurred during the Early Jurassic and Middle Jurassic. Trace-element compositions suggest that Scheelite I was controlled by the coupled substitution reactions of $2Ca^{2+} = Na^{+} + REE^{3+}$ and $Ca^{2+} + W^{6+} = Nb^{5+} + REE^{3+}$, whereas Scheelite II was controlled by the coupled reactions of $2Ca^{2+} = Na^{+} + REE^{3+}$ and $3Ca^{2+} = \square Ca + 2REE^{3+}$ (where □ is a site vacancy). High Mo and low Ce contents suggest that both Scheelite I and Scheelite II were precipitated from oxidizing magmatic-hydrothermal fluids. Based on the mineral assemblage of the altered granite-type ores and geochemical characteristics of Scheelite I [i.e., negative Eu anomalies (0.02–0.05; mean = 0.03 and STD = 0.01), and high $^{87}Sr/^{86}Sr$ ratios (0.70939–0.71932; mean = 0.71345 and STD = 0.00245)], we infer that fluid-rock interaction played an important role in modifying Early Jurassic ore-forming fluids. Scheelite II exhibits a geochemical composition [i.e., $^{87}Sr/^{86}Sr$ ratios (0.70277–0.71471; mean = 0.70940 and STD = 0.00190), Eu anomalies (0.14–0.55; mean = 0.26 and STD = 0.09), and Y/Ho ratios (16.1–33.7; mean = 27.9 and STD = 2.91)] similar to that of the Middle Jurassic Guposhan granites, suggesting inheritance of these features from granite-related magmatic-hydrothermal fluids. These results provide new insights into the two-stage magmatic and metallogenic history of the Nanling Range during the Jurassic Period.

Keywords: scheelite; Re–Os dating; U–Pb dating; W–Sn mineralization; Guposhan

1 INTRODUCTION

The South China, well-known for its huge resources of tungsten–tin (W–Sn) and other rare metals, is one of the most significant metallogenic domains in the world (Fig. 1; Mao et al. 2007, 2008, 2013; Chen et al. 2013; Hu et al. 2017; Cao et al. 2018a, 2018b, 2020a; Zhou et al. 2018; Li et al. 2019a; Tang et al. 2019; Xie et al. 2019a, 2019b). Its estimated tungsten and tin reserves are 8,050,000 tons and 5,956,000 tons, respectively (Fu et al. 2017a). Several large to super-large W–Sn polymetallic deposits occur in the Nanling Range, with the most representative being the Shizhuyuan, Xihuashan, Piaotang, Yaogangxian, Furong, Xianghualing, Taoxikeng, Dengfuxian and Xitian deposits (Fig. 1; Peng et al. 2006; Yuan et al. 2008, 2011; Guo et al. 2011; Hu et al. 2012; Zhang et al. 2017; Cao et al. 2018a, 2018b; Li et al. 2019b; Jiang et al. 2019; Tang et al. 2020). The ages of these ore deposits mostly range from 165 to 150 Ma, e.g., Xihuashan (157.8 ± 0.9; Hu et al. 2012), Piaotang (159.8 ± 0.3; Zhang et al. 2017), Yaogangxian (154.9 ± 2.6; Peng et al. 2006), Xitian (156.6 ± 0.7 Ma; Cao et al. 2018a) and Furong (159.9 ± 1.9; Yuan et al. 2011), and are similar to the ages of Middle Jurassic felsic granites in this region (Mao et al. 2007; Li et al. 2017; Jiang et al. 2018a, 2018b; Cao et al. 2018a, 2018b). Recently, using laser ablation inductively coupled plasma-mass spectrometer (LA–ICP–MS) zircon U–Pb dating technology, numerous Early Jurassic felsic intrusions were identified in the Nanling Range, which include the Wengang granite (192 ± 1 Ma; Zhu et al. 2010), the Hanhu granodiorite (193 ± 2 Ma; Yu et al. 2010), the Xialan granite (196 ± 2 Ma; Yu et al. 2010), the Dabaoshan

granodiorite (175.8 ± 1.5 Ma; Wang et al. 2011), and the Tiandong granite (188 ± 1 Ma; Zhou et al. 2018). However, none of these intrusions was associated with W–Sn mineralization. Recently, the ore-forming age of the Dading Fe–Sn deposit in the southeastern Nanling Range was reported at 185.9 ± 1.2 Ma, using Ar–Ar isotopic dating technology on phlogopite from stratiform skarn-type ore bodies (Cheng et al. 2016; Fig. 1). This was the first Early Jurassic mineralization event reported from the Nanling Range, and it was corroborated by a molybdenite Re–Os age of 185.9 ± 4.9 Ma for the skarn-type ore bodies in this deposit (Zhao et al. 2019). These ages are also consistent with a U–Pb zircon age of 187.5 ± 1.8 Ma (Cheng et al. 2016) and a zircon U–Pb of 189.0 ± 1.5 Ma for the related Shibei granitic pluton (Zhao et al. 2019). Hence, the Early Jurassic granitoids of the Nanling Range provide insight into not only the Early Jurassic magmatism of this region but also its contemporaneous metallogenic evolution.

As one of the major W-bearing minerals, scheelite ($CaWO_4$) occurs not only in quartz vein-, skarn-, greisen- and altered granite-type W deposits but also in hydrothermal Au, Sn and Mo deposits (Ghaderi et al. 1999; Brugger et al. 2002; Guo et al. 2016; Hazarika et al. 2016; Raju et al. 2016; Fu et al. 2017b; Mackenzie et al. 2017; Orhan 2017; Liu et al. 2019; Sciuba et al. 2019). Scheelite commonly contains significant amounts of rare earth elements (REEs), Mo, Nb, Na and Sr via substitution for Ca or W in the crystal structure, and these components provide clues to the source, physico-chemical conditions, and evolutionary history of the ore-forming fluids (Raimbault et al. 1993; Ghaderi et al. 1999; Brugger et al. 2000, 2002, 2008; Song et al. 2014; Kozlik et al. 2016). Recently, laser ablation multiple collector inductively coupled plasma mass spectrometry (LA–MC ICP–MS) has been widely used to measure the trace-element and Sr–Nd isotopic compositions of scheelite (e.g., Fu et al.

2017b; Sun and Chen 2017; Peng et al. 2018; Zhao et al. 2018; Liu et al. 2019; Sun et al. 2019). This technique is an ideal tool to study tungsten mineralization in order to constrain the source and physico-chemical conditions of the ore-forming fluids as well as fluid-rock interaction processes.

The Guposhan district, located in the southwestern Nanling Range, is famous for its large-scale W–Sn mineralization, with estimated tungsten and tin reserves of 59,2000 tons and 687,000 tons, respectively (Fu et al. 2017a). Previous studies reported only Middle Jurassic ages for the granitic magmatism and related W–Sn mineralization in the Guposhan ore district. In this study, we report LA–ICP–MS zircon U–Pb and molybdenite Re–Os ages for the Helukou W deposit, northern Guposhan district that document a two-stage (Early and Middle Jurassic) history of granitic magmatism and related W–Sn mineralization in the Nanling region. In addition, the *in-situ* trace-element and Sr isotopic compositions of scheelite from the skarn-type and altered granite-type ores of the Helukou W deposit constrain the nature of the ore-forming fluids in this magmatic-hydrothermal system.

2 REGIONAL AND ORE DEPOSIT GEOLOGY

2.1 Regional geology

The South China Craton is composed of the Yangtze Block in the northwest and Cathaysia Block in the southeast (Fig. 1). The Nanling Range, located in the central part of the Cathaysia Block, is one of the largest metallogenic belts in China and is characterized by giant W–Sn, and other rare metal deposits (Hua et al. 2005, 2007; Mao et al. 2007; Hu et al. 2012, 2017; Chen et al. 2013; Chen et al. 2016; Cao et al. 2018b; Wu et al. 2018; Li et al. 2018a, 2018b, 2018c). In this region, the stratigraphic succession consists of metamorphosed Proterozoic-Lower Paleozoic siliciclastic and

volcanic rocks, overlain by Upper Paleozoic-Mesozoic carbonate and siliciclastic rocks (Cao et al. 2018b). These units were deformed tectonically, which produced folds and faults widely across the Nanling Range (Wang et al. 2003, 2013; Mao et al. 2007, 2008, 2013). In addition, Mesozoic tectonic events exerted great influence on this region, leading to development of E–W-trending faults and folds before the Middle Jurassic (i.e., during the Indosinian Orogeny) and NE-trending faults after the Middle Jurassic (i.e., during subduction of Paleo-Pacific Plate) (Shu et al. 2004; Mao et al. 2007). Jurassic intrusives (165–150 Ma), which are widespread in the Nanling Range, are composed of granitic and minor mafic rocks (Mao et al. 2008, 2011). These intrusives are highly fractionated and originated from partial melting of Proterozoic basement rocks of the South China Craton (Chen et al. 2013; Li et al. 2014a, 2014b; Cao et al. 2018b).

The Guposhan ore district, located in the southwestern Nanling Range, hosts a series of W–Sn deposits such as the Helukou, Shuiyuanba, and Xinlu deposits (Fig. 2; Li et al. 2015). The ore mineralization ages of these deposits are 160–165 Ma, consistent with the age of the Guposhan granitic pluton (Gu et al. 2007; Li et al. 2015; Cao et al. 2020b). Gu et al. (2007) proposed the division of the Guposhan pluton into three units, namely the East unit (160.8 ± 1.6 Ma), the West unit (165.0 ± 1.9 Ma), and the Lisong unit (163.0 ± 1.3 Ma). The outcropping granites in the northern part of the Guposhan ore field belong to the West unit (Fig. 2) and consist mainly of fine-grained and medium-fine-grained biotite granites.

2.2 Ore deposit geology

The Helukou W deposit, with total estimated tungsten reserves of > 33,752 tons, is located in southwestern Hunan Province (northeastern Guposhan district; Fig. 2). The outcropping strata in the mining district mainly consist of Devonian shallow-marine

siliciclastic and carbonate rocks (Fig. 3a) belonging to the Tiaomajian, Huanggongtang, and Qiziqiao formations (Zeng et al. 2008). The Huanggongtang Formation comprises dolomite and impure limestones, and hosts the main ore-bearing strata for the skarn-type W ore bodies (Fig. 3b; Zeng et al. 2008). Faults in the mining district can be classified into two groups: NW-SE-trending and quasi-N-S-trending faults, with the latter being the main ore-controlling structures (Fig. 3a; Zeng et al. 2008). Hydrothermal alteration processes affecting these deposits include skarnization, greisenization, sericitization, silicification, and albitization, although skarnization and albitization are primarily associated with the skarn-type and altered granite-type W deposits, respectively. Magmatic rocks mainly consist of medium to fine-grained biotite granites with ages of 165.0 ± 1.9 Ma (Gu et al. 2007).

A total of 33 tungsten ore veins, mainly skarn-type and altered granite-type, were identified in this deposit. The non-exposed altered granite-type ore bodies, which consist of scheelite-bearing disseminated ore, are hosted by the upper domain of the Early Jurassic granites (Fig. 4a–4b). The main ore minerals are scheelite, molybdenite, pyrite, ilmenite, magnetite and galena (Fig. 5a–5d), and gangue minerals include K-feldspar, quartz, fluorite and calcite (Fig. 5a–5d). Scheelite in the altered granite-type ore bodies (Scheelite I) occurs as xenomorphic and/or subhedral crystals, has grain sizes of 0.01–0.91 mm, and exhibits intergrown textures with plagioclase, fluorite and quartz (Fig. 5a–5d).

The dominant skarn-type ore bodies, which comprise more than 75% of the total tungsten reserves, are found mainly within the endo- and exo-contact zones between Devonian Huanggongtang Formation carbonates and Middle Jurassic Guposhan granites (Fig. 4c). These stratiform and/or lenticular ore bodies are mostly NE-trending, with a length of 50–750 m, a thickness of 1–107 m, and a WO_3 grade of 0.06–0.70%.

169 The scheelite- and molybdenite-bearing skarns with massive structure are composed
170 mainly of garnet, epidote and vesuvianite (Fig. 4d–4i). Ore minerals of the skarn-type
171 deposits consist mainly of scheelite, molybdenite, pyrite, chalcopyrite, galena, ilmenite
172 and xenotime (Fig. 5e–5i), and gangue minerals include hessonite, andradite, almandine,
173 K-feldspar, apatite, quartz, fluorite and zircon (Fig. 5e–5i). Scheelite in the skarn-type
174 ores (Scheelite II) is xenomorphic-subhedral, has grain sizes of 0.08–3.0 mm, and
175 displays intergrown textures with garnet, epidote and vesuvianite (Fig. 5e–5i).

176 # 3 SAMPLING AND ANALYTICAL TECHNIQUES

177 ## 3.1 Sample collection and description

178 Granites and skarn-type ore samples were collected from mining tunnels of the
179 Helukou W deposit, whereas samples of the altered granite-type ores were collected
180 from drill cores (Fig. 3a). Prior to mineral chemical analyses, thin sections of rock and
181 ore samples were prepared and photographed using optical and backscattered electron
182 (BSE) microscopy. For LA–ICP–MS U–Pb dating, zircon grains were taken from three
183 samples including a fine-grained muscovite granite (Sample No. HLK-1-1), a fine-
184 grained biotite granite (Sample No. HLK-6), and an altered granite-type ore (Sample
185 No. HLK-3). For Re–Os dating, molybdenite grains were separated from six skarn-type
186 and two altered granite-type ore samples. Additionally, scheelites from altered granite
187 type- (Scheelite I) and skarn type-ores (Scheelite II) were chosen for *in-situ* LA–ICP–
188 MS trace-element analyses and *in-situ* LA–MC–ICP–MS Sr isotopic analyses.

189 The fine-grained muscovite granites are light grey in color, have a massive
190 structure and porphyritic texture, and contain K-feldspar (~38%), plagioclase (~25%),
191 quartz (~30%), muscovite (~5%) and hornblende (~2%), with zircon, apatite, titanite,
192 sphene, magnetite and ilmenite as accessory minerals (Fig. 6a–6c). The medium-fine-

grained biotite granites have a massive structure and porphyritic texture, and contain K-feldspar (~30%), plagioclase (~15%), quartz (~45%), and biotite (~8%) and hornblende (~2%), with zircon, apatite, titanite, sphene, magnetite and ilmenite as accessory minerals (Fig. 6d–6f).

3.2 Cathodoluminescence (CL) imaging

Zircon and scheelite grains were separated by conventional magnetic and heavy liquid techniques and hand-picked using a binocular microscope at the Wuhan Sample Solution Analytical Technology Co., Ltd. (Wuhan, China). They were then mounted in epoxy resin blocks and polished to obtain flat surfaces. CL imaging permitted observation of the internal structures of individual zircon and scheelite grains, using a scanning electron microscope (SEM) housed at the Key Laboratory of Crust-Mantle Materials and Environments, Chinese Academy of Sciences, University of Science and Technology of China (Hefei, China). The imaging condition was 10.0–13.0 kV voltage, 80–85 μA current, and two minutes for imaging.

3.3 Zircon U–Pb dating

U–Pb age determinations were performed using a LA–ICP–MS system at the Mineral Geochemistry Lab, Ore Deposit and Exploration Centre (ODEC), Hefei University of Technology (Hefei, China). An Agilent 7900 Quadrupole ICP-MS coupled to a Photon Machines Analyte HE 193-nm ArF Excimer laser ablation system was used for the analyses. Zircon 91500 and synthetic silicate glass NIST SRM610 were applied as external standards for U–Pb dating and trace-element analyses, respectively. Helium was used as a carrier gas to enhance the transport efficiency of the ablated material, and argon was used as the make-up gas and mixed with helium in the ablation cell before injection into the ICP to maintain stable and optimum excitation

conditions. The flow rate of helium was set at 0.6 L/min and a laser beam of 32 μm in diameter with an ablation depth of about 20 μm was adopted. U–Pb ages of zircon were calculated based on U decay constants of $^{238}U = 1.55125 \times 10^{-10}$ year^{-1} and $^{235}U = 9.8454 \times 10^{-10}$ year^{-1} (Jaffey et al. 1971). The 91500 standard was dated at 1062 ± 6.6 Ma in this experiment, which is consistent with a previously reported age of 1062 ± 4 Ma for 91500 (Wiedenbeck et al. 1995). Analytical errors for individual samples are presented as 1σ in Table 1, whereas uncertainties in weighted mean ages are quoted at 2σ (95% confidence) in concordia diagrams. The measurement accuracy was better than 96% (2σ). Quantitative calibrations for zircon U–Pb dating and trace-elements were performed by ICPMSDataCal 10.7 (Liu et al. 2010). Common Pb was corrected based on the model of Andersen (2002). Weighted mean age calculations and concordia diagrams were generated using Isoplot 3.0 (Ludwig 2003).

3.4 Molybdenite Re–Os dating

Molybdenite grains were first separated with a knife and then hand-picked under a binocular microscope. The procedures of powdered sample digestion, Os distillation and Re extraction were conducted following the methods described by Stein et al. (2001) and Du et al. (2004). The Re and Os isotope ratios were determined using an inductively coupled plasma mass spectrometer (TJA X-series ICP-MS) at the National Research Center of Geoanalysis, Chinese Academy of Geological Sciences (Beijing, China). The molybdenite standard GBW04435 (HLP) was used to test analytical reproducibility. The uncertainty for individual age determinations, representing the sum of uncertainties associated with the decay constant of ^{187}Re, isotope ratio measurements, and spike calibrations, was about 0.02%. Average blanks for the total Carius tube procedure were ca. 10 pg Re and ca. 1 pg Os. The Re–Os isochron age was calculated using Isoplot 3.0 (Ludwig, 2003). The decay constant used in the age calculation was $\lambda^{187}Re = 1.666 \times$

242 10^{-11} $year^{-1}$ (Smoliar et al., 1996).

243 **3.5 *In-situ* LA–ICP–MS trace-element analysis of scheelite**

244 Trace-element analysis of scheelite was conducted by LA-ICP-MS at the Wuhan
245 Sample Solution Analytical Technology Co., Ltd. (Wuhan, China). Detailed operating
246 conditions for the laser ablation system and the ICP-MS instrument and data reduction
247 are the same as given in Zong et al. (2017). Laser sampling was performed using a
248 GeolasPro laser ablation system consisting of a COMPexPro 102 ArF excimer laser
249 (wavelength of 193 nm and maximum energy of 200 mJ) and a MicroLas optical
250 system. An Agilent 7700e ICP-MS instrument was used to acquire ion-signal
251 intensities. Helium was used as the carrier gas, and argon was used as the make-up gas
252 and mixed with the carrier gas via a T-connector before injection into the ICP. A "wire"
253 signal smoothing device was included in this laser ablation system (Hu et al. 2015). The
254 spot size and frequency of the laser were set to 32 μm and 5 Hz, respectively. Trace-
255 element compositions of minerals were calibrated against various reference materials
256 (BHVO-2G, BCR-2G, and BIR-1G) without using an internal standard (Liu et al.
257 2008). Each analysis incorporated a background acquisition of approximately 20-30 s
258 followed by 50 s period of sample data acquisition. The measurement accuracy was
259 better than 97% (1σ). An Excel-based software ICPMSDataCal was used to perform
260 off-line selection and integration of background and analyzed signals, time-drift
261 correction, and quantitative calibrations (Liu et al. 2008).

262 **3.6 *In-situ* LA–MC–ICP–MS strontium isotopic analysis of scheelite**

263 Sr isotopic measurements of scheelite were performed using a Neptune Plus MC-
264 ICP-MS (Thermo Fisher Scientific, Bremen, Germany) in combination with a Geolas
265 HD excimer ArF laser ablation system (Coherent, Göttingen, Germany) at the Wuhan

Sample Solution Analytical Technology Co., Ltd. (Wuhan, China). The Neptune Plus was equipped with nine Faraday cups fitted with 1011 Ω resistors. The Faraday collector configuration of the mass system was composed of an array from L4 to H3 to monitor Kr, Rb, Er, Yb, and Sr. A combination of a high-sensitivity X-skimmer cone and Jet-sample cone was employed. In the laser ablation system, helium was used as the carrier gas for the ablation cell. For single-spot laser ablation, the spot diameter ranged from 60 to 160 μm depending on Sr signal intensity. The pulse frequency was from 8 to 15 Hz, and the laser fluence was held constant at ~10 J/cm^2. The data reduction for LA–MC–ICP–MS analysis was conducted using ICPMSDataCal (Liu et al. 2010). The interference correction strategy was the same as that reported by Tong et al. (2016). The regions of integration for both gas background and sample were initially selected, and no additional Kr peak stripping was applied following the background correction, which removed the background Kr+ signals. Then, interferences were corrected in the following sequence: (1) interferences of $^{168}Er^{++}$ on ^{84}Sr, $^{170}Er^{++}$ and $^{170}Yb^{++}$ on ^{85}Rb, $^{172}Yb^{++}$ on ^{86}Sr, and $^{174}Yb^{++}$ on ^{87}Sr were corrected based on the measured signal intensities of $^{167}Er^{++}$, $1^{73}Yb^{++}$ and the natural isotope ratios of Er and Yb (Berglund and Wieser 2011); and (2) the isobaric interference of ^{87}Rb on ^{87}Sr was corrected by monitoring the ^{85}Rb signal intensity and a user-specified $^{87}Rb/^{85}Rb$ ratio using an exponential law for mass bias. The user-specified $^{87}Rb/^{85}Rb$ ratio was calculated by measuring some reference materials with a known $^{87}Sr/^{86}Sr$ ratio. Following the interference corrections, mass fractionation of Sr isotopes was corrected by assuming $^{88}Sr/^{86}Sr = 8.375209$ (Tong et al. 2016) and applying the exponential law. Two natural apatite crystals (Durango and MAD) were used as unknown samples for *in-situ* Sr isotopic analyses of apatite. The uncertainty of the $^{88}Sr/^{86}Sr$ ratio (2σ) for single measurements was 0.0003–0.0004. The analyzed $^{88}Sr/^{86}Sr$ ratios of Durango and

MAD crystals in this study are 0.706346 ± 0.000516 and 0.711879 ± 0.000157, respectively, which are within error of the reported ratios of 0.71180 and 0.70632, respectively (Yang et al. 2014).

4. RESULTS

4.1 Zircon U–Pb ages

LA–ICP–MS zircon U–Pb age data for two granites and one altered granite type ore sample from the Helukou W deposit are reported in Table 1. Most zircon grains from the fine-grained muscovite granite (HLK-1-1) are euhedral, have lengths of 100–200 μm and aspect ratios of 1:1 to 3:1, and show internal oscillatory zoning, suggesting a magmatic origin (Hoskin and Schaltegger 2003; Fig. 7). The Th and U contents of these zircon grains are 147-458 ppm and 252-1340 ppm, respectively, with Th/U ratios of 0.25–0.79 (mean = 0.48 and STD = 0.09). Sixteen analyses of magmatic domains are plotted on the concordia diagrams. The grains yield $^{206}Pb/^{238}U$ ages ranging from 162 to 169 Ma (Table 1), with a weighted average of 163.8 ± 1.5 Ma (MSWD = 0.41; Fig. 8a–b). This age can be interpreted as the crystallization age of the fine-grained muscovite granite.

Zircon grains from the altered granite-type ore (HLK-3) are mostly euhedral or subhedral and have lengths of 150–200 μm and aspect ratios of 1:1–3:1. CL imaging revealed that the cores of these zircons show internal oscillatory zoning but the grain margins did not, with clear boundaries between the edges and cores (Fig. 7). This pattern suggests that these zircons experienced metamictization, i.e., in which fluids altered the structure of grain margins to varying degrees (Rivanova et al. 2000; Liatti, et al. 2002). These zircon grains have variable Th (152–2500 ppm) and U contents (397–9018 ppm), yielding Th/U ratios of 0.25–0.64 (mean = 0.38 and STD = 0.10).

Based on their petrographic and Th/U characteristics, these zircons are inferred to have a magmatic origin, and the U-Pb dates represent their crystallization age, although they have experienced various degrees of hydrothermal alteration. Twelve analyses of magmatic domains yield concordant $^{206}Pb/^{238}U$ and $^{207}Pb/^{235}U$ ratios and plot on or close to the concordia curve (Fig. 8c). The $^{206}Pb/^{238}U$ ages of these zircon grains range from 177 to 185 Ma (Table 1), yielding a weighted average age of 181.5 ± 2.1 Ma (MSWD = 0.75; Fig. 8d).

Zircon grains from the fine-grained biotite granite (HLK-6) are mostly euhedral, have lengths of 50–200 μm and aspect ratios of 1:1–4:1, and display internal oscillatory zoning, indicating a magmatic origin (Hoskin and Schaltegger 2003; Fig. 7). These grains have variable Th (79.2–1206 ppm) and U contents (181–7488 ppm), with Th/U ratios of 0.16–0.49 (mean = 0.36 and STD = 0.06). Eleven of the magmatic zircons have concordant $^{206}Pb/^{238}U$ and $^{207}Pb/^{235}U$ ratios when plotted on concordia diagrams (Fig. 8e). The $^{206}Pb/^{238}U$ ages of these zircons range from 180 to 189 Ma (Table 1), yielding a weighted average $^{206}Pb/^{238}U$ age of 184.0 ± 3.6 Ma (MSWD = 0.15; Fig. 8f). This age can be considered as the crystallization age of the fine-grained biotite granite.

4.2 Molybdenite Re–Os ages

The Re–Os isotopic compositions of molybdenite samples from the Helukou tungsten deposit are given in Supplementary Table 2. The total Re, ^{187}Re and ^{187}Os contents of six molybdenite samples from the skarn-type ores vary from 10238 to 48518 ppb, 6436 to 30494 ppb, and 18.5 to 85.2 ppb, respectively, yielding a ^{187}Re-^{187}Os isochron age of 163.4 ± 2.8 Ma (MSWD = 0.71; Fig. 9a). These samples have invariant Re–Os model ages ranging from 162.9 Ma to 171.9 Ma, yielding a weighted average age of 168.9± 2.8 Ma (MSWD = 3.5; Fig. 9b). These ages indicate that the skarn-type tungsten mineralization was related to Middle Jurassic granitic magmatism.

Two molybdenite samples from the altered granite-type ore have total Re, ^{187}Re and ^{187}Os contents of 9914–30434 ppb, 6231–19129 ppb, and 18.4–57.9 ppb, respectively, yielding an isochron age of 183.5 ± 2.8 Ma (Fig. 9c). In addition, the model ages of these samples are 176.9 Ma and 181.4 Ma, respectively, yielding a weighted mean age of 179.3 ± 6.7 Ma (MSWD = 8.1; Fig. 9d). This age is consistent with the zircon age of the fine-grained biotite granite, indicating that the altered granite-type tungsten deposit was related to Early Jurassic granitic magmatism.

4.3 Trace-element compositions of scheelite

The trace-element compositions of scheelite from the Helukou tungsten deposit are given in Table 3. Scheelite I has Na, Sr, Nb, and Mo contents of 18.7–96.3 ppm (mean 38.7 ppm, STD = 18.3 ppm), 98.9–128 ppm (mean 113 ppm, STD = 6.46 ppm), 124–480 ppm (mean 188 ppm, STD = 61.6 ppm), and 4419–6973 ppm (mean 5245 ppm, STD = 622 ppm), respectively. Relative to it, Scheelite II (skarn-type ore) has higher and more variable Na contents (8.6–184 ppm, mean = 87.6 ppm, STD =39.4 ppm) and lower Sr, Nb, and Mo contents (32.8–128 ppm, mean 55.6 ppm, STD = 12.7 ppm; 22.7–447 ppm, mean 124 ppm, STD = 59.8 ppm; and 646–3496 ppm, mean 2280 ppm, STD = 497 ppm, respectively). Both Scheelite I and Scheelite II have relatively low Rb concentrations (mostly <0.1 ppm).

In terms of rare earth element (REE) compositions, Scheelite II has higher and more variable ΣREE (267–2272 ppm; mean 1059 ppm and STD = 594 ppm) than Scheelite I (347–724 ppm; mean 467 ppm and STD = 80.1 ppm). Both Scheelite I and Scheelite II have negative Eu anomalies (Eu/Eu* = 0.02–0.05 and 0.14–0.55, respectively) and slight positive Ce anomalies (Ce/Ce* = 1.08–1.20 and 1.20–1.45, respectively; Fig. 10).

4.4 Strontium isotopic compositions of scheelite

The strontium isotopic compositions of scheelite from the Helukou tungsten deposit are given in Table 4. The $^{87}Sr/^{86}Sr$ ratios of Scheelite I and Scheelite II vary from 0.70939 to 0.71932 and 0.70277 to 0.71471, respectively (Fig. 11). In addition, both Scheelite I and Scheelite II have relatively low $^{87}Rb/^{86}Sr$ ratios, ranging from 0.00149 to 0.02030 and from 0.00351 to 0.07324, respectively.

5. DISCUSSION

5.1 Timing of W–Sn mineralization in the Nanling Range

Previous studies reported that the Guposhan pluton is Middle Jurassic in age with an early-stage granite at 165.0 ± 1.9 Ma and a late-stage granite at 154.2 ± 3.1 Ma (Gu et al. 2007; Wang et al. 2014). In the present study of the Helukou deposit (NE Guposhan district; Fig. 2), a zircon U–Pb age of 163.8 ± 1.5 Ma for fine-grained muscovite granite conforms to published ages for the early-stage Guposhan granites (Gu et al. 2007). Furthermore, a Re–Os age of 163.4 ± 2.8 Ma for molybdenite from the skarn-type tungsten ore is consistent with Ar–Ar ages of ca. 160 Ma for other tungsten deposits in the northern Guposhan ore field (Li et al. 2015).

The Early Jurassic (205–180 Ma) has long been regarded as an interval of magmatic and metallogenic quiescence in the Nanling Range (Zhou et al. 2006; Jiang et al. 2008). However, recent studies have provided evidence of Early Jurassic magmatism, and some have reported related tungsten and/or tin mineralization events (Yu et al. 2010; Zhu et al. 2010; Wang et al. 2011; Zhou et al. 2018; Zhao et al. 2019). In the present study, a zircon U–Pb age of 184.0 ± 3.6 Ma and a molybdenite Re–Os age of 183.5 ± 2.8 Ma demonstrate coeval magmatism and tungsten mineralization in the Guposhan ore district during the Early Jurassic. Therefore, our new data, coupled

with previously reported ages, suggest two stages of magmatism (~184 Ma and ~164 Ma) and two stages of W–Sn mineralization (~180 Ma and ~163 Ma) in the Helukou tungsten deposit of the Guposhan ore field. These findings provide new evidence for links between Early Jurassic magmatism and tungsten mineralization in the Nanling Range, suggesting an extended interval of W mineralization and a potential metallogenic era in this region.

5.2 REE substitution reactions

The ionic radii of trivalent REEs are similar to that of bivalent Ca, and, therefore, REE^{3+} can enter the lattice of scheelite through substitution for Ca^{2+} (Ghaderi et al., 1999). The most important coupled substitution reactions between REE^{3+} and Ca^{2+} are as follows (Ghaderi et al., 1999):

$$2Ca^{2+} = Na^{+} + REE^{3+} \quad \text{(Eq. 1)}$$

$$Ca^{2+} + W^{6+} = Nb^{5+} + REE^{3+} \quad \text{(Eq. 2)}$$

$$3Ca^{2+} = \square Ca + 2REE^{3+}, \text{ where } \square \text{ is a site vacancy} \quad \text{(Eq. 3)}$$

In terms of reaction (1), if Na provides the charge balance in scheelite, MREEs preferentially enter the lattice by substitution in the Ca site because of their similar ionic radii, which results in MREE-rich patterns and high Na concentrations (Ghaderi et al. 1999; Brugger et al. 2002). Reaction (2) results in Nb concentrations that are high and nearly equal to ΣREE content (Dostal et al. 2009). Reaction (3) leads to a relatively flat chondrite-normalized REE pattern (Ghaderi et al. 1999). In the present study, both Scheelite I and Scheelite II have relatively high Na contents, ranging from 18.7 to 96.3 ppm and from 39.3 to 184 ppm, respectively, indicating that reaction (1) is a likely candidate, an inference supported by enrichment of Scheelite I in MREEs (Fig. 10a). Furthermore, some samples of Scheelite II plot along the 1:1 line between Na (atom)

and REE+Y-Eu (atom), also supporting operation of reaction (1) during formation of Scheelite II (Fig. 12a).

Reaction (2) was not important in the study units, as shown by the Nb contents of Scheelite I and Scheelite II (137 to 480 ppm and 22.7 to 447 ppm, respectively) being lower than their REEs concentrations. Also significant is that Scheelite I plots near the 1:1 line of Nb (atom) and REE+Y-Eu (atom), whereas Scheelite II plots away from the 1:1 line (Fig. 12b). The strong positive correlation between Na+Nb (atom) and REE+Y-Eu (atom) for Scheelite I indicates control of substitutions by coupled reactions (1) and (2) (Fig. 12c). On the other hand, the similar correlations between Na + Nb (atom) and REE+Y-Eu (atom) and between Na (atom) and REE+Y-Eu (atom) for Scheelite II suggest that reaction (2) can be ruled out for this mineral phase (Fig. 12a and 12c). However, because Scheelite II does not show a strong positive correlation between Na (atom) and REE+Y-Eu (atom), REE substitution in Scheelite II is unlikely to have been controlled exclusively by reaction (1). Scheelite II is characterized by relatively flat chondrite-normalized REE patterns inherited from the source fluids, supporting the operation of reaction (3) in this mineral phase.

5.3 Geochemical significance of scheelite

Ce can enter the scheelite lattice as either Ce^{3+} or Ce^{4+} along with other REE^{3+} ions, but Ce^{3+} enters the scheelite lattice more easily than Ce^{4+} because of the similar ionic radii of Ce^{3+} (1.14 Å) and Ca^{2+} (1.12 Å) (Shannon 1976; Gaderi et al. 1999; Sun et al. 2019). Therefore, scheelite precipitated from oxidizing fluids tend to contain low Ce concentrations. Mo concentrations in scheelite can also be a sensitive tracer of the redox conditions of the ore-forming fluids (Raimbault et al. 1993; Rempel et al. 2009). Under oxidizing conditions, Mo^{6+} readily enters the scheelite lattice via substitution for W^{6+}, leading to Mo enrichment (Raimbault et al. 1993; Rempel et al. 2009). In contrast,

under reducing conditions, Mo^{4+} does not substitute easily for W^{6+} in scheelite, resulting in low Mo contents. Both Scheelite I and Scheelite II have high Mo contents, 646–3496 ppm (mean 2280 ppm) and 4419–6973 ppm (mean 5245 ppm) (Fig. 12d), respectively, which accords with the high Mo concentrations of scheelite in the nearby giant Zhuxi tungsten deposit (prograde skarn stage; 1171–3291 ppm; Sun et al. 2019). Furthermore, negative covariation of Mo and Ce in both Scheelite I and Scheelite II supports oxidizing conditions in the ore-forming fluids (Fig. 12e).

Due to the similar ionic radii and valences of Y and Ho, Y/Ho ratios tend to remain fairly stable in a given magmatic-hydrothermal system, allowing their use as a fluid source indicator (Bau and Dulski 1995; Bau 1996; Irber 1999). Relatively invariant Y/Ho ratios are shown by both Scheelite I (16.9–24.3, mean 19.3) and Scheelite II (16.1–33.7, mean 27.9). In addition, both Scheelite I and Scheelite II exhibit strong positive correlations between Y and Ho (R^2 = 0.99 and 0.86, respectively (Fig. 12f), indicating that these two mineral phases were precipitated from a single source fluid. In addition, it should be noted that the Y/Ho ratios of Scheelite II are consistent with previously published Y/Ho ratios (28–35) for the Middle Jurassic Guposhan granites (Wang et al. 2014).

Both Scheelite I and Scheelite II have high Sr concentrations and low Rb concentrations, yielding negligibly low Rb/Sr ratios, suggesting that the ^{87}Sr produced by radioactive decay of ^{87}Rb can be ignored and the measured $^{87}Sr/^{86}Sr$ ratios of scheelite can be equated with initial ratios at the time of crystallization or element redistribution (Kozlik et al. 2016). However, the relatively high $^{87}Sr/^{86}Sr$ ratios of Scheelite I (0.70939–0.71932) may not represent the initial $^{87}Sr/^{86}Sr$ compositions of the Early Jurassic granites, since fluid-rock interaction may have altered the $^{87}Sr/^{86}Sr$ compositions of the primary magmatic-hydrothermal fluids. Fluid-rock interaction

462 between fluids and Early Jurassic granites is indicated by extremely negative Eu
463 anomalies (Eu/Eu* = 0.02–0.05), which are much lower than those of granitic rocks in
464 the Guposhan region (Wang et al. 2014). The precipitation of abundant K-feldspar from
465 a granitic melt can consume substantial Eu, leading to Eu depletion of the fluid and a
466 large negative Eu anomaly, as seen in Scheelite I. In addition, fluid-rock interaction
467 may have resulted in hydrolyzation of mica minerals in the Early Jurassic granites,
468 leading to release of Rb and higher $^{87}Rb/^{86}Sr$ ratios in the ore-forming fluids, which
469 finally elevated their $^{87}Sr/^{86}Sr$ ratios through production of radiogenic ^{87}Sr (Glodny and
470 Grauert, 2009; Kozlik et al., 2016; Cao et al. 2020c). The $^{87}Sr/^{86}Sr$ ratios of Scheelite II
471 (0.70277–0.71471) are in good agreement with those of the ore-related Middle Jurassic
472 Guposhan granites (Fig. 11; Gu et al. 2007). Together with the similar Eu anomalies of
473 Scheelite II (0.14–0.55) and the Middle Jurassic ore-forming granites (0.09–0.57) and
474 their relatively flat chondrite-normalized REE patterns, the Sr isotope data indicate that
475 Scheelite II inherited the REE signature of the fluids from which it formed, and that
476 these signatures represent the initial $^{87}Sr/^{86}Sr$ compositions of Middle Jurassic granites
477 in the Guposhan region. Thus, scheelite that crystallizes from primary magmatic-
478 hydrothermal fluids not experiencing intense fluid-rock interactions can retain the Sr
479 isotopic signature of the related granites, providing a new tool to constrain genetic
480 relationships between scheelite and ore-related granites.

481 # 6. IMPLICATIONS

482 1) Our study provides evidence of two-stage magmatism and related tungsten
483 mineralization in the Guposhan region, i.e., an Early Jurassic (~180 Ma) event and a
484 Middle Jurassic (~163 Ma) event, expanding the known temporal range of these

processes and the ore-prospecting potential in the Nanling Range, since the Early Jurassic tungsten mineralization in Nanling range is poorly known to date.

2) Trace elements and Sr isotopes of scheelite can be a good tool to reveal the physical-chemical conditions of ore-forming fluids and to demonstrate genetic relationships between scheelite and ore-related granites.

ACKNOWLEDGMENTS

This work was financed by the National Key Research and Development Plan (Grant No. 2018YFC0603902).

REFERENCES

Andersen, T. (2002) Correction of common lead in U–Pb analyses that do not report ^{204}Pb. Chemical Geology, 192, 59–79.

Bau, M. (1996) Controls on the fractionation of isovalent trace elements in magmatic and aqueous systems: evidence from Y/Ho, Zr/Hf, and lanthanide tetrad effect. Contributions to Mineralogy and Petrology, 123, 323–333.

Bau, M., and Dulski, P. (1995) Comparative study of yttrium and rare-earth element behaviours in fluorine-rich hydrothermal fluids. Contributions to Mineralogy and Petrology, 119, 213-223.

Berglund, M., and Wieser, M.E. (2011) Isotopic compositions of the elements 1997 (IUPAC Technical Report). Pure and Applied Chemistry, 83, 397–410.

Brugger, J., Etschmann, B., Pownceby, M., Liu, W., Grundler, P., and Brewe, D. (2008) Oxidation state of europium in scheelite: tracking fluid–rock interaction in gold deposits. Chemical Geology, 257, 26–33.

Brugger, J., Lahaye, Y., Costa, S., Lambert, D., and Bateman, R. (2000) Inhomogeneous distribution of REE in scheelite and dynamics of Archaean

509 hydrothermal systems (Mt. Charlotte and Drysdale gold deposits, Western
510 Australia). Contributions to Mineralogy and Petrology, 139, 251–264.
511 Brugger, J., Maas, R., Lahaye, Y., Mcrae, C., Ghaderi, M., Costa, S., Lambert, D.,
512 Bateman, R., and Prince, K. (2002) Origins of Nd–Sr–Pb isotopic variations in
513 single scheelite grains from Archaean gold deposits, Western Australia. Chemical
514 Geology, 182, 203–225.
515 Cao, J.Y., Wu, Q.H., Yang, X.Y., Deng, X.T., Li, H., Kong, H., and Xi, X.S. (2020a)
516 Geochemical factors revealing the differences between the Xitian and Dengfuxian
517 composite plutons, middle Qin-Hang Belt: Implications to the W–Sn
518 mineralization. Ore Geology Reviews, 118, 103353
519 Cao, J.Y., Wu, Q.H., Yang, X.Y., Kong, H., Li, H., Xi, X.S., Huang, Q.H., and Liu, B.
520 (2018a) Geochronology and genesis of the Xitian W–Sn polymetallic deposit in
521 eastern Hunan Province, South China: Evidence from zircon U–Pb and muscovite
522 Ar–Ar dating, petrochemistry, and wolframite Sr–Nd–Pb isotopes. Minerals 8, art.
523 111.
524 Cao, J.Y., Yang, X.Y., Du, J.G., Wu, Q.H., Kong, H., Li, H., Wan, Q., Xi, X.S., Gong,
525 Y.S., and Zhao, H.R. (2018b) Formation and geodynamic implication of the Early
526 Yanshanian granites associated with W–Sn mineralization in the Nanling range,
527 South China: an overview. International Geology Review, 60, 1744–1771.
528 Cao, J.Y., Yang, X.Y., Lu, Y.Y., Fu, J.M., and Yang, L.Z. (2020b) Zircon U–Pb and Sm–
529 Nd geochronology and geochemistry of the Sn–Wdeposits in the northern
530 Guposhan ore field, Nanling Range, southern China. Ore Geology Reviews, 118,
531 103323.
532 Cao, J.Y., Yang, X.Y., Zhang, D.X., and Yan, F.B. (2020c) In situ trace elements and Sr
533 isotopes in scheelite and S-Pb isotopes in sulfides from the Shiweidong W–Cu

deposit, giant Dahutang ore field:Implications to the fluid evolution and ore genesis. Ore Geology Reviews, 125, 103696.

Chen, J., Wang, R.C., Zhu, J.C., Lu, J.J., and Ma, D.S. (2013) Multiple-aged granitoids and related tungsten-tin mineralization in the Nanling Range, South China. Science in China D: Earth Sciences, 56, 2045–2055 (in Chinese with English abstract).

Cheng, S.B., Fu, J.M., Ma, L.Y., Lu, Y.Y., Wang, X.D., and Xia, J.L. (2016) Early Jurassic iron-tin mineralization event in the Nanling Range: Evidence from LA-ICP-MS zircon U-Pb and phlogopite $^{39}Ar/^{40}Ar$ dating of the Dading deposit in Lianping, Northern Guangdong. Acta Geologica Sinica, 90, 163–176 (in Chinese with English abstract).

Du, A.D., Wu, S.Q., Sun, D.Z., Wang, S.X., Qu, W.Q., Markey, R., Stain, H., Morgan, J., and Malinovskiy, D. (2004) Preparation and certification of Re–Os dating reference materials: molybdenites HLP and JDC. Geostandards and Geoanalytical Research, 28, 41–52.

Fu, J.M., Lu, Y.Y., and Niu, Z.J. (2017a) Nanling metallogenic belt. Atomic Energy Press, Beijing, 2, 6–7. (in Chinese)

Fu, Y., Sun, X., Zhou, H., Lin, H., Jian, L., and Yang, T. (2017b) In-situ LA–ICP–MS trace elements analysis of scheelites from the giant Beiya gold-polymetallic deposit in Yunnan province, Southwest China and its metallogenic implications. Ore Geology Reviews, 80, 828–837.

Ghaderi, M., Palin, J.M., Campbell, I.H., and Sylvester, P.J. (1999) Rare earth element systematics in scheelite from hydrothermal gold deposits in the Kalgoorlie-Norseman region, Western Australia. Economic Geology, 94, 423–437.

Glodny, J., and Grauert, B. (2009) Evolution of a hydrothermal fluid-rock interaction

559 system as recorded by Sr isotopes: A case study from the Schwarzwald, SW
560 Germany. Mineralogy and Petrology, 95, 163–178.
561 Gu, S.Y., Hu, R.M., and Qi, H.W. (2007) Zircon LA–ICP–MS U–Pb dating and Sr–Nd
562 isotope study of the Guposhan granite complex, Guangxi, China. Chinese Journal
563 of Geochemistry, 26, 290–300.
564 Guo, C.L., Mao, J.W., Bierlein, F., Chen, Z.H., Chen, Y.C., Li, C.B., and Zeng, Z.L.
565 (2011) SHRIMP U–Pb (zircon), Ar–Ar (muscovite) and Re–Os (molybdenite)
566 isotopic dating of the Taoxikeng tungsten deposit, south China Block. Ore
567 Geology Reviews, 43, 26–39.
568 Guo, Z.J., Li, J.W., Xu, X.Y., Song, Z.Y., Dong, X.Z., Tian, J., Yang, Y.C., She, H.Q.,
569 Xiang, A.P., and Kang, Y.J. (2016) Sm–Nd dating and REE composition of
570 scheelite for the Honghuaerji scheelite deposit, Inner Mongolia, Northeast
571 China. Lithos, 261, 307–321.
572 Hazarika, P., Mishra, B., and Pruseth, K.L. (2016) Scheelite, apatite, calcite and
573 tourmaline compositions from the late Archean Hutti orogenic gold deposit:
574 implications for analogous two stage ore fluids. Ore Geology Reviews, 72, 989–
575 1003.
576 Hoskin, P.W.O., and Schaltegger, U. (2003) The composition of zircon and igneous
577 and metamorphic petrogenesis. Reviews in Mineralogy and Geochemistry, 53, 27–
578 62.
579 Hu, R.Z., Chen, W.T., Xu, D.R., and Zhou, M.F. (2017) Reviews and new metallogenic
580 models of mineral deposits in South China: An introduction. Journal of Asian
581 Earth Sciences, 137, 1–118.
582 Hu, R.Z., Wei, W.F., Bi, X.W., Peng, J.T., Qi, Y.Q, Wu, L.Y., and Chen, Y.W. (2012)
583 Molybdenite Re–Os and muscovite $^{40}Ar/^{39}Ar$ dating of the Xihuashan tungsten

584 deposit, central Nanling district, South China. Lithos, 150, 111–118.

585 Hu, Z.C., Zhang, W., Liu, Y.S., Gao, S., Li, M., Zong, K.Q., Chen, H.H., and Hu, S.H.
586 (2015) "Wave" signal smoothing and mercury removing device for laser ablation
587 quadrupole and multiple collector ICP–MS analysis: application to lead isotope
588 analysis. Analytical Chemistry, 87, 1152–1157.

589 Hua, R.M., Chen, P.R., Zhang, W.L., and Lu, J.J. (2005) Three major metallogenic
590 events in Mesozoic in South China. Mineral Deposits, 24, 99–107 (in Chinese with
591 English abstract).

592 Hua, R.M., Zhang, W.L., Gu, S.Y., and Chen, P.R. (2007) Comparison between REE
593 granites and W–Sn granite in the Nanling region, South China, and their
594 mineralizations. Acta Petrologica Sinica, 23, 2321–2328 (in Chinese with English
595 abstract).

596 Irber, W. (1999) The lanthanide tetrad effect and its correlation with K/Rb, Eu/Eu*,
597 Sr/Eu, Y/Ho, and Zr/Hf of evolving peraluminous granite suites. Geochimica et
598 Cosmochimica Acta, 63, 489–508.

599 Jaffey, A.H., Flynn, K.F., Glendenin, L.E., Bentley, W.C., and Essling, A.M. (1971)
600 Precision measurement of half-lives and specific activities of ^{235}U and ^{238}U.
601 Physical Review C, 4, 1889–1906.

602 Jiang, S.Y., Zhao, K.D., Jiang, Y.H., and Dai, B.Z. (2008) Characteristics and genesis
603 of Mesozoic A-type granites and associated mineral deposits in the southern
604 Hunan and northern Guangxi provinces along the Shi-Hang belt, South China.
605 Geological Journal of China Universities, 14, 496–509 (in Chinese with English
606 abstract).

607 Jiang, W.C., Li, H., Evans, N.J., Wu, J., and Cao, J.Y. (2018b) Metal sources of world-
608 class polymetallic W–Sn skarns in the Nanling Range, South China: Granites

versus sedimentary rocks? Minerals, 8, 265. https://doi.org/10.3390/min8070265.

Jiang, W.C., Li, H., Mathur, R., and Wu, J.H. (2019) Genesis of the giant Shizhuyuan W–Sn–Mo–Bi–Pb–Zn polymetallic deposit, South China: Constraints from zircon geochronology and geochemistry in skarns. Ore Geology Reviews, 111, art. 102980, 22 pp., https://doi.org/10.1016/j.oregeorev. 2019.102980.

Jiang, W.C., Li, H., Wu, J.H., Zhou, Z.K., Kong, H., and Cao, J.Y. (2018a) A newly found biotite syenogranite in the Huangshaping polymetallic deposit, South China: Insights into Cu mineralization. Journal of Earth Science, 29, 537–555.

Kozlik, M., Gerdes, A., and G. Raith, J. (2016) Strontium isotope systematics of scheelite and apatite from the Felbertal tungsten deposit, Austria—Results of in-situ LA–MC–ICP–MS analysis. Mineralogy and Petrology, 110, 11–27.

Li, C., Zhou, L.M., Zhao, Z., Zhang, Z.Y., Zhao, H., Li, X.W., and Qu, W.J. (2018) In-situ Sr isotopic measurement of scheelite using fs–LA–MC–ICPMS. Journal of Asian Earth Sciences, 160, 38–47.

Li, H., Cao, J.Y., Algeo, T.J., Jiang, W.C., Liu, B., and Wu, Q.H. (2019b) Zircons reveal multi-stage genesis of the Xiangdong (Dengfuxian) tungsten deposit, South China. Ore Geology Reviews, 111, 102979.

Li, H., Kong, H., Zhou, Z.K., Wu, Q.H., Xi, X.S., and Gabo-Ratio, J.A.S. (2019a) Ore-forming material sources of the Jurassic Cu–Pb–Zn mineralization in the Qin–Hang ore belt, South China: Constraints from S–Pb isotopes. Geochemistry, 79, 280–306.

Li, H., Palinkaš, L.A., Watanabe, K., and Xi, X.S. (2018c) Petrogenesis of Jurassic A-type granites associated with Cu–Mo and W–Sn deposits in the central Nanling region, South China: Relation to mantle upwelling and intra-continental extension. Ore Geology Reviews, 92, 449–462.

Li, H., Sun, H.S., Algeo, T.J., Wu, J.H., Cao, J.Y., and Wu, Q.H. (2018a) Mesozoic multi-stage W–Sn polymetallic mineralization in the Nanling Range, South China: An example from the Dengfuxian–Xitian ore field. Geological Journal, 54, 3755–3785.

Li, H., Watanabe, K., and Yonezu, K. (2014a) Zircon morphology, geochronology and trace element geochemistry of the granites from the Huangshaping polymetallic deposit, South China: Implications for the magmatic evolution and mineralization processes. Ore Geology Reviews, 60, 14–35.

Li, H., Watanabe, K., and Yonezu, K. (2014b) Geochemistry of A–type granites in the Huangshaping polymetallic deposit (South Hunan, China): Implications for granite evolution and associated mineralization. Journal of Asian Earth Sciences, 88, 149–167.

Li, H., Wu, J.H., Evans, N.J., Jiang, W.C., and Zhou, Z.K. (2018b) Zircon geochronology and geochemistry of the Xianghualing A-type granitic rocks: Insights into multi-stage Sn-polymetallic mineralization in South China. Lithos, 312–313, 1–20.

Li, S.Z., Zang, Y.B., Wang, S.P., Suo, Y.H., Li, X,Y., Liu, X., Zhou, Z.Z., Liu, X.G., and Wang, Q. (2017) Mesozoic tectonic transition in South China and initiation of Palaeo-Pacific subduction. Earth Science Frontiers, 24, 213–225 (in Chinese with English abstract).

Li, X., Xiao, R., Feng, Z., Wei, C.X., Tang, Y., Bai, Y., and Zhang, M. (2015) Ar–Ar Ages of hydrothermal muscovite and igneous biotite at the Guposhan-Huashan District, Northeast Guangxi, South China: Implications for Mesozoic W–Sn mineralization. Resource Geology, 65, 160–176.

Liati, A., Gebauer, D., and Wysoczanski, R. (2002) U–Pb SHRIMP- dating of zircon

domains from UHP garnet- rich mafic rocks and late pegmatoids in the Rhodope zone (N Greece): Evidence for Early Cretaceous crystallization and Late Cretaceous metamorphism. Chemical Geology, 184, 281–299

Liu, B., Li, H., Wu, Q.H., Evans, N.J., Cao, J.Y, Jiang, J.B., and Wu, J.H. (2019) Fluid evolution of Triassic and Jurassic W mineralization in the Xitian ore field, South China: Constraints from scheelite geochemistry and microthermometry. Lithos, 330, 1–15.

Liu, Y.S., Gao, S., Hu, Z., Gao, C., Zong, K., and Wang, D. (2010) Continental and oceanic crust recycling-induced melt-peridotite interactions in the Trans-North China Orogen: U–Pb dating, Hf isotopes and trace elements in zircons from mantle xenoliths. Journal of Petrology, 51, 537–571.

Liu, Y.S., Hu, Z.C., Gao, S., Günther, D., Xu, J., Gao, C.G., and Chen, H.H. (2008) In situ analysis of major and trace elements of anhydrous minerals by LA–ICP–MS without applying an internal standard. Chemical Geology, 257, 34–43.

Ludwig, K.R. (2003) ISOPLOT 3.00: A Geochronological Toolkit for Microsoft Excel. Berkeley Geochronology Center, Berkeley, California, 39 pp.

Mackenzie, D., Farmer, L., Moore, J., and Craw, D. (2017) Contrasting coeval paragenesis of gold and scheelite in an orogenic hydrothermal system, Macraes mine, New Zealand. Ore Geology Reviews, 80, 645–657.

Mao, J.W., Cheng, Y.B., Chen, M.H., and Pirajno, F. (2013) Major types and time-space distribution of Mesozoic ore deposits in South China and their geodynamic settings. Mineralium Deposita, 48, 267–294.

Mao, J.W., Xie, G.Q., Guo, C.L, Yuan, S.D., Cheng, Y.B., and Chen, Y.C. (2008) Spatial-temporal distribution of Mesozoic ore deposits in south China and their metallogenic settings. Geological Journal of China Universities, 14, 510–526 (in

Chinese with English abstract).

Mao, J.W., Xie, G.Q., Guo, C.L., and Chen, Y.C. (2007) Large-scale tungsten-tin mineralization in the Nanling region, South China: Metallogenic ages and corresponding geodynamic processes. Acta Petrologica Sinica, 23, 2329–2338 (in Chinese with English abstract).

Orhan, A. (2017) Evolution of the Mo-rich scheelite skarn mineralization at Kozbudaklar, western Anatolia, Turkey: Evidence from mineral chemistry and fluid inclusions. Ore Geology Reviews, 80, 141–165.

Peng, J.T., Zhou, M.F., Hu, R.Z., Shen, N.P., Yuan, S.D., Bi, X.W., Du, A.D., Qu, and W.J. (2006) Precise molybdenite Re-Os and mica Ar-Ar dating of the Mesozoic Yaogangxian tungsten deposit, central Nanling district, South China. Mineralium Deposita, 41, 661–669.

Peng, N.J., Jiang, S.Y., Xiong, S.F., and Pi, D.H. (2018) Fluid evolution and ore genesis of the Dalingshang deposit, Dahutang W-Cu ore field, northern Jiangxi Province, South China. Mineralium Deposita, 53, 1079–1094.

Raimbault, L., Baumer, A., Dubru, M., Benkerrou, C., Crozen, V., and Zahm, A. (1993) REE fractionation between scheelite and apatite in hydrothermal conditions. American Mineralogist, 78, 1275–1285.

Raju, P.V.S., Hart, C.J.R., and Sangurmath, P. (2016) Scheelite geochemical signatures by LA–ICP–MS and potential for rare earth elements from Hutti gold mines and fingerprinting ore deposits. Journal of African Earth Sciences, 114, 220–227.

Rempel, K.U., Williams-Jones, A.E., and Migdisov, A.A. (2009) The partitioning of molybdenum (VI) between aqueous liquid and vapour at temperatures up to 370 °C. Geochimica et Cosmochimica Acta, 73, 3381–3392.

Rizvanova, N.G., Lenchenkov, O.A., Belous, A.E., Bezmen, N.I., Maslenikov, A.V.,

Komarov, A.N., Makeev, A.F., and Levskiy, L.K. (2000) Zircon reaction and stability of the U- Pb isotope system during the interaction with carbonate fluid: Experimental hydrothermal study. Contribution to Mineralogy and Petrology, 139, 101– 134

Shannon, R.D. (1976) Revised effective ionic radii and systematic studies of interatomic distances in halides and chalcogenides. Acta Crystallographica, 32, 751–767.

Shu, L.S., Zhou, X.M., Deng, P., Yu, X.Q., Wang, B., and Zu, F.P. (2004) Geological features and tectonic evolution of MesoCenozoic basins in southeastern China. Geological Bulletin of China, 23, 876–884 (in Chinese with English abstract).

Smoliar, M.I., Walker, R.J., and Morgan, J.W. (1996) Re-Os ages of Group IIA, IIIA, IVA, and IVB iron meteorites. Science, 271, 1099–1102.

Song, G.X., Qin, K.Z., Li, G.M., Evans, N.J., and Chen, L. (2014) Scheelite elemental and isotopic signatures: implications for the genesis of skarn-type W–Mo deposits in the Chizhou area, Anhui province, eastern China. American Mineralogist, 99, 303–317.

Stein, H.J., Markey, R.J., Morgan, J.W., Hannah, J.L., and Schersten, A. (2001) The remarkable Re–Os chronometer in molybdenite: how and why it works. Terra Nova, 13, 479–486.

Sciuba, M., Beaudoin, G., Grzela, D. and Makvandi, S., (2019) Trace element composition of scheelite in orogenic gold deposits. Mineralium Deposita, 55, 1–24.

Sun, K.K., and Chen, B. (2017) Trace elements and Sr–Nd isotopes of scheelite: Implications for the W–Cu–Mo polymetallic mineralization of the Shimensi deposit, South China. American Mineralogist, 102, 1114–1128.

Sun, K.K., Chen, B., and Deng, J. (2019) Ore genesis of the Zhuxi supergiant W-Cu skarn polymetallic deposit, South China: Evidence from scheelite geochemistry. Ore Geology Reviews, 107, 14–29.

Taylor, S.R., and McLennan, S.M. (1985) The Continental Crust: Its Composition and Evolution, Blackwell Scientific Publications, Oxford.

Tang, C., Yang, X.Y., and Cao, J.Y. (2019) Genesis of the Shangjinshan W–Mo polymetallic deposit in the Eastern Jiangnan tungsten belt: Evidences from geochemistry, geochronology and zircon Hf isotope analyses. Ore Geology Reviews, 115, 103172.

Tang, Y.W., Cui, K., Zheng, Z., Gao, J.F., Han, J.J., Yang, J.H., and Liu, L. (2020) LA-ICP-MS UPb geochronology of wolframite by combining NIST series and common lead-bearing MTM as the primary reference material:Implications for metallogenesis of South China. Gondwana Research, 83, 217–230.

Tong, X.R., Liu, Y.S., Hu, Z.C., Chen, H.H., Zhou, L., Hu, Q.H., Xu, R., Deng, L.X., Chen, C.F., and Yang, L. (2016) Accurate ddetermination of Sr isotopic compositions in clinopyroxene and silicate glasses by LA–MC–ICP–MS. Geostandards and Geoanalytical Research, 40, 85–99.

Wang, L., Hu, M.G., Yang, Z., Qu, W.J., Xia, J.L., and Chen, K.X. (2011) U–Pb and Re–Os geochronology and geodynamic setting of the Dabaoshan polymetallic deposit, northern Guangdong Province, South China. Ore Geology Reviews, 43, 40–49.

Wang, Y.J., Fan, W.M., Guo, F., Peng, T.P., and Li, C.W. (2003) Geochemistry of Mesozoic Mafic Rocks adjacent to the Chenzhou-Linwu fault, South China: Implications for the lithospheric boundary between the Yangtze and Cathaysia Blocks. International Geology Review, 45, 263–286.

759 Wang, Y.J., Fan, W.M., Zhang, G.W., and Zhang, Y.H. (2013) Phanerozoic tectonics
760 of the South China Block: Key observations and controversies. Gondwana
761 Research, 23, 1273–1305.
762 Wang, Z.Q., Chen, B., and Ma, X. (2014) Petrogenesis of the Late Mesozoic Guposhan
763 composite plutons from the Nanling Range, South China: Implications for W–Sn
764 mineralization. American Journal of Science, 314, 235–277.
765 Wiedenbeck, M., Alle, P., Corfu, F., Griffin, W.L., Meier, M., Ober, F., Von Quadt, A.,
766 Roddick, J.C., and Speigel, W. (1995) Three natural zircon standards for U–Th–
767 Pb, Lu–Hf, trace-element and REE analyses. Geostandards Newsletter: the Journal
768 of Geostandards and Geoanalysis, 19, 1–23.
769 Wu, J.H., Li, H., Algeo, T.J., Jiang, W.C., and Zhou, Z.K. (2018) Genesis of the
770 Xianghualing Sn–Pb–Zn deposit, South China: A multi-method zircon study. Ore
771 Geology Reviews, 102, 220–239.
772 Xie, G.Q., Mao, J.W., Bagas, L., Fu, B., and Zhang, Z.Y. (2019b) Mineralogy and
773 titanite geochronology of the Caojiaba W deposit, Xiangzhong metallogenic
774 province, southern China: implications for a distal reduced skarn W formation.
775 Mineralium Deposita, 54, 459–472.
776 Xie, G.Q., Mao, J.W., Li, W., Fu, B., Zhang, Z.Y. (2019a) Granite-related Yangjiashan
777 tungsten deposit, southern China. Mineralium Deposita, 54, 67–80.
778 Yang, Y.H., Wu, F.Y., Yang, J.H., Chew, D.M., Xie, L.W., Chu, Z.Y., Zhang, Y.B.,
779 and Huang, C. (2014) Sr and Nd isotopic compositions of apatite reference
780 materials used in U–Th–Pb geochronology. Chemical Geology, 385, 35–55.
781 Yu, X.Q., Wu, G.G., Zhao, X.X., Gao, J.F., Di, Y.J., Zheng, Y., Dai, Y.P., Li, C.L., and
782 Qiu, J.T. (2010) The Early Jurassic tectono-magmatic events in southern Jiangxi
783 and northern Guangdong provinces, SE China: Constraints from the SHRIMP

784 zircon U–Pb dating. Journal of Asian Earth Sciences, 39, 408-422.
785 Yuan, S., Peng, J., Hao, S., Li, H., Geng, J., and Zhang, D. (2011) In situ LA–MC–
786 ICP–MS and ID–TIMS U–Pb geochronology of cassiterite in the giant Furong tin
787 deposit, Hunan Province, South China: New constraints on the timing of tin–
788 polymetallic mineralization. Ore Geology Reviews, 43, 235–242.
789 Yuan, S., Peng, J., Hu, R., Li, H., Shen, N., and Zhang, D. (2008) A precise U–Pb age
790 on cassiterite from the Xianghualing tin-polymetallic deposit (Hunan, South
791 China). Mineralium Deposita, 43, 375–382.
792 Yuan, S.D., Peng, J.T., Hao, S., Li, H.M., Geng, J.Z., and Zhang, D.L. (2011) In situ,
793 LA–MC–ICP–MS and ID–TIMS U–Pb geochronology of cassiterite in the giant
794 Furong tin deposit, Hunan Province, South China: New constraints on the timing
795 of tin–polymetallic mineralization: Ore Geology Reviews, 43, 235–242.
796 Zeng, Z.F., Zeng, G.X., and Zeng, Y.H. (2008) Ore-controlling structures and
797 metallogenesis in the Guposhan tungsten-tin field, Hunan province. Geology and
798 Prospecting, 44, 1–7 (in Chinese with English abstract).
799 Zhang, R.Q., Lu, J.J., Lehmann, B., Li, C.Y., Li, C.Y., Zhang, L.P., Guo, J., and Sun,
800 W.D. (2017) Combined zircon and cassiterite U-Pb dating of the Piaotang granite-
801 related tungsten-tin deposit, southern Jiangxi tungsten district, China. Ore
802 Geology Reviews, 82, 268–284.
803 Zhao, P.L., Zhao, H.J., Yuan, S.D., and Mao, J.W. (2019) The Early Jurassic Fe-Sn
804 metallogenic event and its geodynamic setting in South China: Evidence from Re-
805 Os, U-Pb geochronology and geochemistry of the Dading magnesian skarn Fe-Sn
806 deposit. Ore Geology Reviews, 111, 102970.
807 Zhao, W.W., Zhou, M.F., Williams-Jones, A.E., and Zhao, Z. (2018) Constraints on the
808 uptake of REE by scheelite in the Baoshan tungsten skarn deposit, South China.

Chemical Geology, 477, 123–136.

Zhou, M.F., Gao, J.F., Zhao, Z., and Zhao, W.W. (2018) Introduction to the special issue of Mesozoic W-Sn deposits in South China. Ore Geology Reviews, 101, 432–436.

Zhou, X.M., Sun, T., Shen, W.Z., Shu, L.S., and Niu, Y.L. (2006) Petrogenesis of Mesozoic granitoids and volcanic rocks in South China: A response to tectonic evolution. Episodes, 29, 26–33.

Zhou, Z.M., Ma, C.Q., Wang, L.X., Chen, S.G., Xie, C.F., Li, Y., and Liu, W. (2018) A source-depleted Early Jurassic granitic pluton from South China: Implication to the Mesozoic juvenile accretion of the South China crust. Lithos, 300–301, 278–290.

Zhu, W.G., Zhong, H., Li, X.H., He, D.F., Song, X.Y., Ren, T., Chen, Z.Q., Sun, H.S., and Liao, J.Q. (2010) The early Jurassic mafic–ultramafic intrusion and A-type granite from northeastern Guangdong, SE China: Age, origin, and tectonic significance. Lithos, 119, 313–329.

Zong, K.Q., Klemd, R., Yuan, Y., He, Z.Y., Guo, J.L., Shi, X.L., Liu, Y.S., Hu, Z.C., and Zhang, Z.M. (2017) The assembly of Rodinia: The correlation of early Neoproterozoic (ca. 900 Ma) high-grade metamorphism and continental arc formation in the southern Beishan Orogen, southern Central Asian Orogenic Belt (CAOB). Precambrian Research, 290, 32–48.

Zou, J.L., Zeng, Y.H., and Chen, W.H. (2005) Geological characteristics and prospecting potential of the Guposhan tin orefield, southern Hunan province. Geology and Mineral Resource of South China, 2, 45–52. (in Chinese with English abstract)

FIGURE CAPTIONS

FIGURE 1. Geological sketch map of the South China Craton (modified from Zhou et al. 2006), showing the distribution of Mesozoic granitic-volcanic rocks and the Sn-W deposits in the Nanling Range. NLR = Nanling Range.

FIGURE 2. Geological sketch map of Guposhan ore field, showing the location and ages of the Sn–W deposits (modified from Li et al. 2015).

FIGURE 3. (a) Geological sketch map of northern Guposhan ore field, showing the sampling location; (b) No. 30 line geological section of the Helukou deposit (modified from Zou et al. 2005).

FIGURE 4. Photographs of ore bodies and tungsten ores from the Helukou deposit. (a) Hand specimen of altered granite-type ore; (b) Hand specimen of altered granite-type ore showing location of scheelite (under a tungsten lamp); (c) Field photograph showing the contact zone between the Middle Jurassic granites and the skarn-type W ore body; (d) Field photograph of garnet-epidote skarn; (e) Field photograph of garnet-vesuvianite skarn; (f) Field photograph of garnet skarn crossed by quartz vein; (g) Hand specimen of garnet skarn-type ore; (h) Hand specimen of garnet skarn-type ore showing the location of scheelite (under a tungsten lamp); (i) Hand specimen of molybdenite-bearing skarn-type ore.

FIGURE 5. BSE images of skarn-type (a–e) and altered granite-type (f–i) W ores from the Helukou deposit showing the main mineral assemblages. (a) Scheelite coexisting with fluorite and apatite; (b) Xenomorphic scheelite surrounded by fluorite; (c) Fluorite

858 surrounded by euhedral scheelite; (d) Xenomorphic scheelite coexisting with galena
859 and magnetite. (e) Sharp contact between garnet and scheelite; (f) Irregular molybdenite
860 surrounded by andradite; (g) Ilmenite surrounded by xenomorphic scheelite; (h)
861 scheelite coexisting with pyrite; (i) Chalcopyrite and galena surrounded by K-feldspar.
862 Alm–almandine; Ap–apatite; Ard–Andradite; Cal–calcite; Ccp–Chalcopyrite; Fi–
863 fluorite; Gn–galena; Grs–grossular; Ilm–ilmenite; Kfs–K-feldspar; Mag–magnetite;
864 Mo–molybdenite; Py–pyrite; Qtz–quartz; Sch–scheelite; Xtm–xenotime; Zr–zircon.
865
866 **FIGURE 6.** Hand specimens and photomicrographs of granites from the Helukou
867 deposit. (a) Hand specimen of fine-grained muscovite granite; (b–c) Photomicrographs
868 of major mineral assemblages of fine-grained muscovite granite; (d) Hand specimen of
869 fine-grained biotite granite; (e–f) Photomicrographs of major mineral assemblages of
870 fine-grained biotite granite. Bt–biotite; Hbl–hornblende; Kfs–K-feldspar; Pl–
871 plagioclase; Ms–muscovite; Qtz–quartz.
872
873 **FIGURE 7.** Cathodoluminescence (CL) images of representative zircon grains of
874 samples from the Helukou deposit. White circles represent LA–ICP–MS dating spots;
875 yellow lines are boundaries between protogenetic and recrystallized areas of zircon
876 grains.
877
878 **FIGURE 8.** Zircon U–Pb concordia diagram and weighted-mean ages of zircon grains
879 of samples from the Helukou deposit.
880
881 **FIGURE 9.** Molybdenite Re–Os isochron diagram and weighted mean ages of ore
882 samples from the Helukou deposit.
883

884 **FIGURE 10.** Rare earth element distributions in scheelite from the Helukou deposit.
885 Chondrite normalization based on Taylor and McLennan (1985).

886

887 **FIGURE 11.** $^{87}Sr/^{86}Sr$ ratios of scheelite from the Helukou deposit, compared with
888 Middle Jurassic ore-related granites at Guposhan (Gu et al. 2007).

889

890 **FIGURE 12.** (a) Na versus ∑REE + Y–Eu (as 100 atoms per $CaWO_4$ formula unit), (b)
891 Nb versus ∑REE + Y–Eu (as 100 atoms per $CaWO_4$ formula unit), (c) Na + Nb versus
892 ∑REE + Y–Eu (as 100 atoms per $CaWO_4$ formula unit), (d) Eu/ Eu* versus Mo, (e) Mo
893 versus Ce, and (f) Y versus Ho. Note: (a), (b), and (c) are modified from Ghaderi et al.
894 1999).
895

This is the peer-reviewed, final accepted version for American Mineralogist, published by the Mineralogical Society of America.
The published version is subject to change. Cite as Authors (Year) Title. American Mineralogist, in press.
DOI: https://doi.org/10.2138/am-2021-7678. http://www.minsocam.org/

TABLE 1. LA–ICP–MS zircon U–Pb dating data for the granites and altered-granite type ore from the Helukou deposit.

Spot	Th(ppm）	U(ppm）	Th/U	$^{207}Pb/^{206}Pb$		$^{207}Pb/^{235}U$		$^{206}Pb/^{238}U$		$^{208}Pb/^{232}Th$		$^{207}Pb/^{206}Pb$		$^{207}Pb/^{235}U$		$^{206}Pb/^{238}U$	
				Ratio	±1σ	Ratio	±1σ	Ratio	±1σ	Ratio	±1σ	Age (Ma)	±1σ	Age (Ma)	±1σ	Age (Ma)	±1σ
Fine-grained muscovite granite (HLK-1-1)																	
1	147	597	0.25	0.0494	0.0023	0.1734	0.0080	0.0254	0.0004	0.0084	0.0005	165	139.8	162	7.0	162	2.3
2	312	719	0.43	0.0498	0.0022	0.1752	0.0070	0.0255	0.0004	0.0091	0.0003	187	103.7	164	6.0	163	2.4
3	444	560	0.79	0.0492	0.0019	0.1738	0.0067	0.0255	0.0004	0.0077	0.0003	167	88.9	163	5.8	162	2.7
4	458	1340	0.34	0.0497	0.0021	0.1817	0.0062	0.0265	0.0005	0.0090	0.0004	183	96.3	170	5.4	169	3.1
5	336	883	0.38	0.0492	0.0039	0.1765	0.0166	0.0257	0.0009	0.0090	0.0004	154	190.7	165	14.4	164	5.5
6	213	541	0.39	0.0498	0.0040	0.1772	0.0116	0.0259	0.0008	0.0092	0.0004	187	174.0	166	10.0	165	5.2
7	162	275	0.59	0.0500	0.0042	0.1783	0.0124	0.0261	0.0010	0.0092	0.0006	195	194.4	167	10.7	166	6.0
8	193	417	0.46	0.0502	0.0030	0.1745	0.0088	0.0256	0.0008	0.0091	0.0004	211	143.5	163	7.6	163	4.8
9	198	425	0.47	0.0500	0.0024	0.1785	0.0082	0.0260	0.0004	0.0084	0.0003	195	112.9	167	7.1	165	2.5
10	313	601	0.52	0.0486	0.0016	0.1719	0.0056	0.0255	0.0004	0.0076	0.0002	128	77.8	161	4.9	162	2.5
11	152	252	0.60	0.0493	0.0023	0.1745	0.0082	0.0254	0.0004	0.0076	0.0003	161	138.9	163	7.1	162	2.7
12	176	337	0.52	0.0492	0.0033	0.1745	0.0116	0.0255	0.0007	0.0086	0.0005	167	138.9	163	10.1	162	4.2
13	173	334	0.52	0.0495	0.0023	0.1773	0.0085	0.0259	0.0005	0.0082	0.0004	172	109	166	7.3	165	3.0
14	165	311	0.53	0.0498	0.0023	0.1776	0.0083	0.0260	0.0005	0.0085	0.0003	183	114	166	7.1	165	3.1
15	423	902	0.47	0.0496	0.0016	0.1772	0.0059	0.0258	0.0004	0.0075	0.0003	176	78.7	166	5.1	164	2.7
16	208	548	0.38	0.0484	0.0016	0.1747	0.0061	0.0260	0.0004	0.0075	0.0003	120	77.8	163	5.3	166	2.6
Altered granite-type tungsten ore (HLK-3)																	
1	566	1363	0.42	0.0500	0.0013	0.2009	0.0061	0.0290	0.0005	0.0078	0.0002	195	63.0	186	5.2	184	3.0
2	813	1484	0.55	0.0516	0.0022	0.2049	0.0078	0.0289	0.0008	0.0085	0.0003	333	98.1	189	6.6	184	4.9
3	767	1452	0.53	0.0512	0.0019	0.2005	0.0068	0.0284	0.0005	0.0076	0.0002	250	89.8	186	5.8	180	3.1
4	407	1600	0.25	0.0504	0.0013	0.1976	0.0052	0.0283	0.0004	0.0087	0.0003	213	59.2	183	4.4	180	2.6
5	412	1131	0.36	0.0505	0.0014	0.2053	0.0066	0.0293	0.0006	0.0090	0.0003	220	64.8	190	5.6	186	3.7

This is the peer-reviewed, final accepted version for American Mineralogist, published by the Mineralogical Society of America.
The published version is subject to change. Cite as Authors (Year) Title. American Mineralogist, in press.
DOI: https://doi.org/10.2138/am-2021-7678. http://www.minsocam.org/

6	409	1193	0.34	0.0497	0.0029	0.1969	0.0111	0.0287	0.0007	0.0096	0.0005	189	135	182	9.4	182	4.4
7	151	574	0.26	0.0518	0.0031	0.1985	0.0113	0.0278	0.0007	0.0093	0.0007	276	139	184	9.6	177	4.3
8	1032	3481	0.30	0.0513	0.0015	0.2065	0.0084	0.0289	0.0009	0.0093	0.0004	257	66.7	191	7.0	184	5.5
9	126	199	0.64	0.0511	0.0051	0.1998	0.0218	0.0285	0.0008	0.0093	0.0008	256	209	185	18.5	181	5.2
10	282	806	0.35	0.0513	0.0025	0.1957	0.0088	0.0278	0.0007	0.0095	0.0003	254	80.5	181	7.5	177	4.2
11	2500	9018	0.28	0.0516	0.0010	0.2089	0.0052	0.0292	0.0005	0.0089	0.0003	333	38.0	193	4.4	185	3.4
12	129	397	0.32	0.0513	0.0040	0.1991	0.0169	0.0279	0.0007	0.0114	0.0007	254	184.2	184	14.4	177	4.6
Fine-grained biotite granite (HLK-6)																	
1	1206	7488	0.16	0.0501	0.0039	0.1958	0.0136	0.0283	0.0011	0.0139	0.0007	211	181	182	11.5	180	6.7
2	497	1525	0.33	0.0546	0.0022	0.2127	0.0114	0.0290	0.0016	0.0108	0.0004	398	90.7	196	9.6	185	10.3
3	712	2411	0.30	0.0496	0.0022	0.2039	0.0130	0.0297	0.0016	0.0108	0.0007	176	99.1	188	11.0	189	10.2
4	576	1527	0.38	0.0498	0.0060	0.2015	0.0244	0.0293	0.0012	0.0136	0.0006	187	268.5	186	20.6	186	7.3
5	79.2	181	0.44	0.0485	0.0052	0.2017	0.0237	0.0296	0.0012	0.0087	0.0014	120	246	187	20.0	188	7.6
6	174	446	0.39	0.0497	0.0071	0.1979	0.0283	0.0291	0.0015	0.0139	0.0012	183	303.7	183	24.0	185	9.4
7	449	1316	0.34	0.0498	0.0022	0.2019	0.0115	0.0290	0.0009	0.0120	0.0006	187	102	187	9.8	185	5.6
8	178	405	0.44	0.0492	0.0048	0.1974	0.0210	0.0290	0.0013	0.0087	0.0008	167	206	183	17.8	184	7.8
9	268	905	0.30	0.0502	0.0038	0.1984	0.0157	0.0286	0.0009	0.0108	0.0006	206	175.9	184	13.3	182	5.8
10	269	702	0.38	0.0501	0.0027	0.1991	0.0117	0.0286	0.0007	0.0112	0.0005	211	124.1	184	9.9	182	4.5
11	85.5	175	0.49	0.0504	0.0047	0.2010	0.0177	0.0291	0.0008	0.0085	0.0009	213	204	186	14.9	185	5.0
12	483	1219	0.40	0.0509	0.0021	0.2051	0.0089	0.0291	0.0008	0.0091	0.0004	235	92.6	189	7.5	185	4.7

This is the peer-reviewed, final accepted version for American Mineralogist, published by the Mineralogical Society of America.
The published version is subject to change. Cite as Authors (Year) Title. American Mineralogist, in press.
DOI: https://doi.org/10.2138/am-2021-7678. http://www.minsocam.org/

TABLE 2. Molybdenite Re–Os isotopic data for the skarn-type tungsten ore from the Helukou deposit.

Sample No.	Re (ng/g)	2σ	^{187}Re (ng/g)	2σ	^{187}Os ng/g	2σ	T (Ma)	2σ
Molybdenite from the skarn-type tungsten ore								
GPS-1	48518	623	30494	391	85.24	0.586	167.5	2.9
GPS-2	40323	358	25345	225	70.18	0.339	166.0	1.7
GPS-3	41443	609	26048	383	70.80	0.542	162.9	3.1
GPS-4	41778	703	26258	442	72.57	0.451	165.6	3.4
GPS-5	22353	269	14050	169	38.71	0.270	165.1	2.8
GPS-6	10238	45	6436	28	18.46	0.083	171.9	1.08
Molybdenite from the altered granite-type tungsten ore								
AG-1	30434	210	19129	132	57.89	0.421	181.4	1.8
AG-2	9914	73	6231	46	18.39	0.140	176.9	2.6

This is the peer-reviewed, final accepted version for American Mineralogist, published by the Mineralogical Society of America.
The published version is subject to change. Cite as Authors (Year) Title. American Mineralogist, in press.
DOI: https://doi.org/10.2138/am-2021-7678. http://www.minsocam.org/

TABLE 3. LA–ICP–MS trace element compositions of the scheelite from the skarn- and altered granite-type tungsten ore in the Helukou deposit (ppm).

Spot. No	Na	Rb	Sr	Nb	Mo	La	Ce	Pr	Nd	Sm	Eu	Gd	Tb	Dy	Ho	Er	Tm	Yb	Lu	Y	ΣREE	LREE	HREE	δEu	δCe	Y/Ho
Scheelite II																										
1	90.34	0.07	45.9	122	1866	97.7	452	73.0	448	93.0	7.46	96.3	11.8	80.8	13.0	34.2	2.70	11.2	0.67	402	1422	1171	251	0.24	1.25	30.9
2	101.94	0.02	52.5	114	2346	26.1	170	34.9	257	64.9	4.55	76.0	9.06	59.6	9.37	23.3	1.67	6.12	0.38	250	743	557	185	0.20	1.32	26.7
3	89.06	0.00	48.2	43.7	2415	18.6	138	26.7	177	42.5	6.68	44.1	4.85	33.0	4.57	10.9	0.91	2.89	0.14	123	511	409	101	0.47	1.45	27.0
4	8.64	0.02	49.4	206	3496	16.3	106	24.4	192	45.7	1.95	25.2	1.74	8.41	0.92	1.64	0.12	0.54	0.043	27.6	425	387	39	0.18	1.25	30.1
5	13.39	0.04	52.9	27.0	2355	36.7	182	29.9	184	50.7	6.94	68.3	9.84	75.8	12.6	33.5	2.55	9.44	0.47	413	703	491	213	0.36	1.29	32.7
6	13.61	0.02	38.1	22.7	2816	11.9	65.2	11.3	72.9	20.7	2.86	26.3	3.67	27.8	4.72	13.5	1.07	4.77	0.30	145	267	185	82	0.37	1.32	30.7
7	70.33	0.04	63.9	112	1753	293	1108	152	819	149	7.22	135	15.2	94.9	13.5	31.1	2.16	7.09	0.47	454	2827	2528	299	0.16	1.23	33.7
8	39.23	0.01	41.3	96.5	2409	77.6	401	62.8	367	78.9	6.38	85.0	10.8	77.3	12.5	33.3	2.57	10.7	0.61	389	1226	994	233	0.24	1.35	31.1
9	118.20	0.06	65.9	163	1719	12.8	75.7	17.1	141	52.2	3.01	81.8	11.0	76.0	12.0	30.7	2.31	9.86	0.65	313	526	301	224	0.14	1.20	26.1
10	175.26	0.11	60.3	126	1926	82.4	425	69.3	397	72.5	6.08	59.7	6.53	39.3	5.08	11.6	0.84	2.70	0.15	139	1178	1052	126	0.28	1.32	27.4
11	95.03	0.02	54.7	124	2094	131	636	93.1	509	75.3	3.19	60.4	5.96	35.0	5.05	11.7	0.83	2.99	0.16	139	1569	1447	122	0.14	1.35	27.5
12	105.69	0.00	46.7	30.6	2643	17.5	129	25.5	180	44.8	3.65	51.9	6.64	45.4	7.19	19.1	1.31	5.44	0.39	177	538	400	137	0.23	1.43	24.6
13	123.89	0.04	32.8	447	3492	32.2	208	41.8	300	81.0	5.17	104	13.7	96.7	16.5	42.8	3.24	12.6	0.68	462	959	668	290	0.17	1.33	28.0
14	184.24	0.07	128	125	646	356	1081	122	554	141	22.2	110	15.5	98.6	13.3	36.4	4.24	32.9	4.43	214	2591	2276	315	0.55	1.21	16.1
15	85.04	0.03	53.4	94.7	2228	11.8	71.9	15.2	116	39.0	3.50	50.3	6.97	48.6	7.83	22.3	1.88	9.84	0.87	205	406	257	149	0.24	1.26	26.2
Scheelite I																										
1	18.73	0.00	118	180	5720	33.1	126	20.7	115	30.7	0.33	29.2	3.64	17.1	2.76	5.88	0.58	2.15	0.28	60.8	387	326	61.5	0.03	1.13	22.0
2	31.52	0.14	109	165	4778	37.2	148	24.6	129	32.3	0.23	29.5	3.63	16.8	2.84	5.98	0.61	2.17	0.24	60.8	433	371	61.8	0.02	1.14	21.4
3	47.14	0.13	108	168	4419	23.6	126	26.5	171	49.5	0.40	53.0	6.63	30.8	5.50	10.9	1.01	3.22	0.36	92.8	509	397	111.4	0.02	1.18	16.9
4	34.05	0.06	114	174	4721	31.7	141	26.3	156	42.7	0.41	38.9	4.61	21.2	3.23	5.81	0.51	2.07	0.22	58.8	475	399	76.6	0.03	1.14	18.2
5	45.18	0.04	109	137	5637	22.7	123	25.5	169	47.3	0.41	49.7	5.59	26.0	4.02	7.41	0.61	2.43	0.34	71.1	484	388	96.0	0.03	1.19	17.7
6	21.24	0.22	128	174	4672	22.3	96.8	18.7	116	32.0	0.43	35.4	4.72	23.2	4.29	8.62	0.87	3.52	0.41	76.1	367	286	81.0	0.04	1.11	17.7

This is the peer-reviewed, final accepted version for American Mineralogist, published by the Mineralogical Society of America.
The published version is subject to change. Cite as Authors (Year) Title. American Mineralogist, in press.
DOI: https://doi.org/10.2138/am-2021-7678. http://www.minsocam.org/

7	48.56	0.16	111	132	5071	29.2	141	27.5	166	44.6	0.41	43.8	5.15	24.4	3.88	7.65	0.66	2.30	0.26	67.5	497	408	88.1	0.03	1.17	17.4
8	25.01	0.08	122	124	6068	17.7	89.0	18.7	121	32.9	0.42	32.6	3.85	19.0	3.11	5.94	0.65	2.53	0.34	58.9	347	279	68.0	0.04	1.15	18.9
9	96.32	1.25	98.9	141	4983	31.5	159	30.5	180	47.1	0.47	48.0	6.11	31.7	5.35	11.4	1.17	3.89	0.39	98.2	556	448	108	0.03	1.20	18.3
10	37.66	0.00	103	480	4649	20.1	110	25.9	193	91.5	1.21	111	15.5	85.0	15.5	36.1	3.95	14.2	1.41	295	724	441	283	0.04	1.13	19.0
11	19.71	0.03	117	192	6973	42.1	133	19.9	95.2	23.1	0.34	22.3	2.64	13.2	2.28	5.18	0.56	2.33	0.29	55.4	362	314	48.7	0.05	1.08	24.3

This is the peer-reviewed, final accepted version for American Mineralogist, published by the Mineralogical Society of America.
The published version is subject to change. Cite as Authors (Year) Title. American Mineralogist, in press.
DOI: https://doi.org/10.2138/am-2021-7678. http://www.minsocam.org/

TABLE 4. LA–MC–ICP–MS Sr isotopes of the scheelite from the Helukou deposit.

Spot No.	$^{84}Sr/^{86}Sr$	2σ	$^{84}Sr/^{88}Sr$	2σ	$^{87}Rb/^{86}Sr$	2σ	$^{87}Sr/^{86}Sr$	2σ
Scheelite I								
1	0.0575	0.0047	0.00687	0.00056	0.00172	0.000184	0.71142	0.00081
2	0.0572	0.0050	0.00682	0.00059	0.00487	0.000133	0.70939	0.00082
3	0.0571	0.0044	0.00681	0.00052	0.01530	0.005317	0.71698	0.00268
4	0.0585	0.0042	0.00699	0.00050	0.00167	0.000117	0.71281	0.00061
5	0.0499	0.0068	0.00596	0.00081	0.00771	0.000756	0.71507	0.00104
6	0.0578	0.0050	0.00690	0.00059	0.00345	0.000657	0.71271	0.00085
7	0.0595	0.0040	0.00710	0.00048	0.00149	0.000114	0.71210	0.00064
8	0.0557	0.0043	0.00665	0.00052	0.00155	0.000128	0.71125	0.00071
9	0.0551	0.0043	0.00658	0.00051	0.02030	0.000843	0.71932	0.00078
Scheelite II								
1	0.0436	0.0023	0.00520	0.00028	0.01688	0.000266	0.70852	0.00042
2	0.0549	0.0101	0.00655	0.00120	0.00389	0.000253	0.70970	0.00143
3	0.0577	0.0105	0.00689	0.00125	0.00455	0.000295	0.71027	0.00191
4	0.0617	0.0104	0.00737	0.00124	0.00382	0.000297	0.71079	0.00167
5	0.0535	0.0151	0.00639	0.00180	0.00410	0.000397	0.71040	0.00241
6	0.0156	0.0155	0.00186	0.00185	0.07324	0.000467	0.70277	0.00266
7	0.0132	0.0161	0.00158	0.00192	0.06863	0.001111	0.71471	0.00279
8	0.0497	0.0089	0.00593	0.00106	0.00351	0.000217	0.71003	0.00129
9	0.0487	0.0122	0.00582	0.00145	0.00524	0.000342	0.70852	0.00186
10	0.0438	0.0115	0.00523	0.00137	0.00890	0.000442	0.70824	0.00160

This is the peer-reviewed, final accepted version for American Mineralogist, published by the Mineralogical Society of America.
The published version is subject to change. Cite as Authors (Year) Title. American Mineralogist, in press.
DOI: https://doi.org/10.2138/am-2021-7678. http://www.minsocam.org/

Figure 1

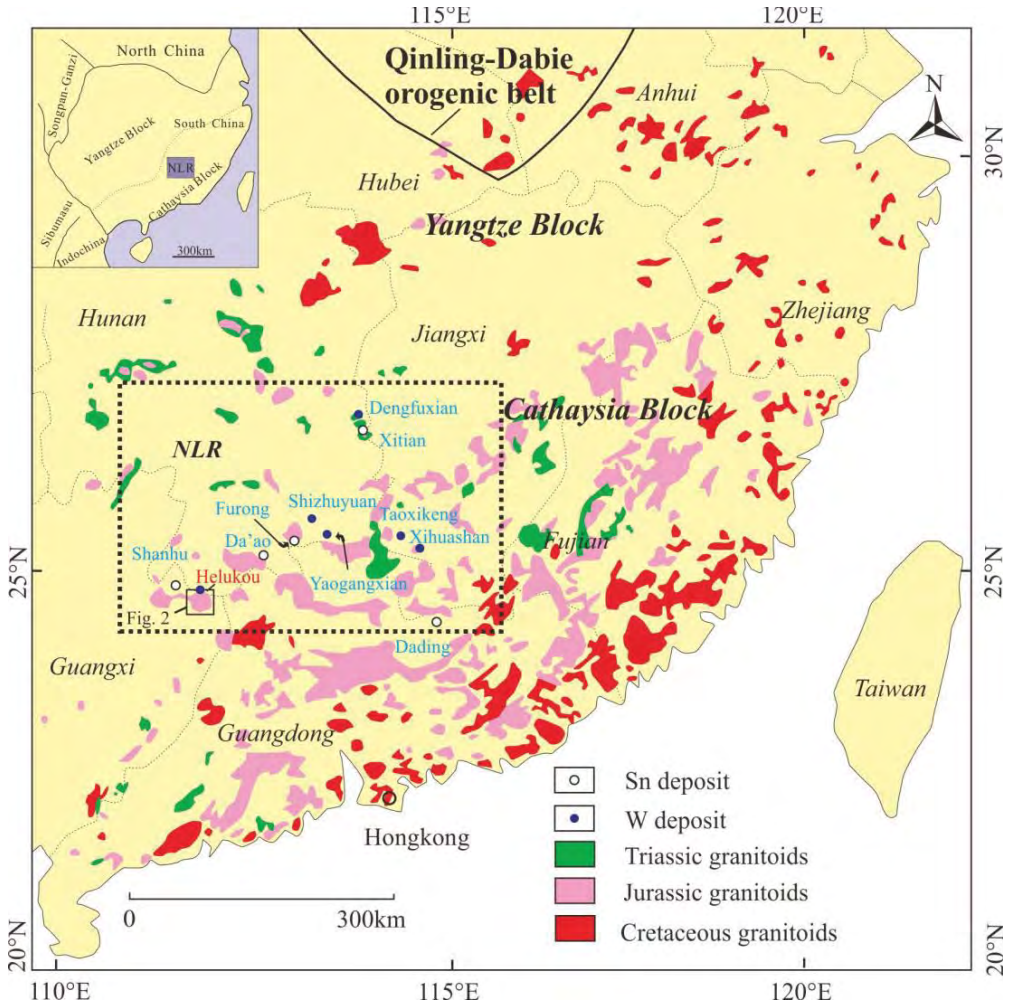

This is the peer-reviewed, final accepted version for American Mineralogist, published by the Mineralogical Society of America.
The published version is subject to change. Cite as Authors (Year) Title. American Mineralogist, in press.
DOI: https://doi.org/10.2138/am-2021-7678. http://www.minsocam.org/

Figure 2

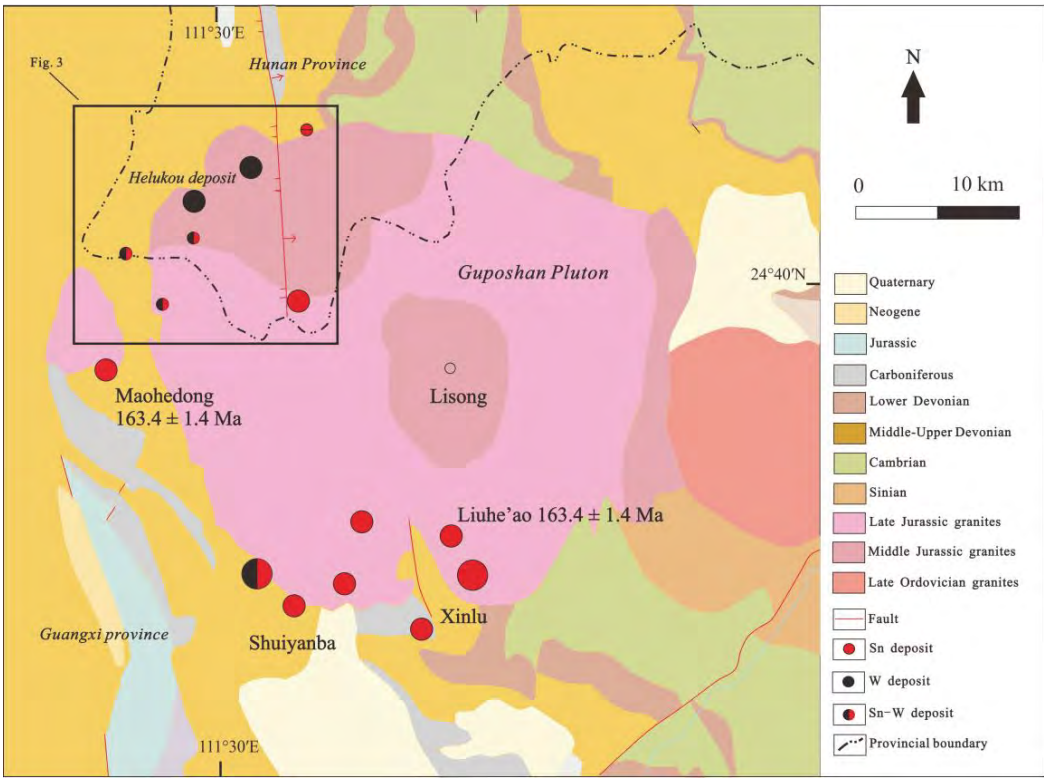

This is the peer-reviewed, final accepted version for American Mineralogist, published by the Mineralogical Society of America.
The published version is subject to change. Cite as Authors (Year) Title. American Mineralogist, in press.
DOI: https://doi.org/10.2138/am-2021-7678. http://www.minsocam.org/

Figure 3

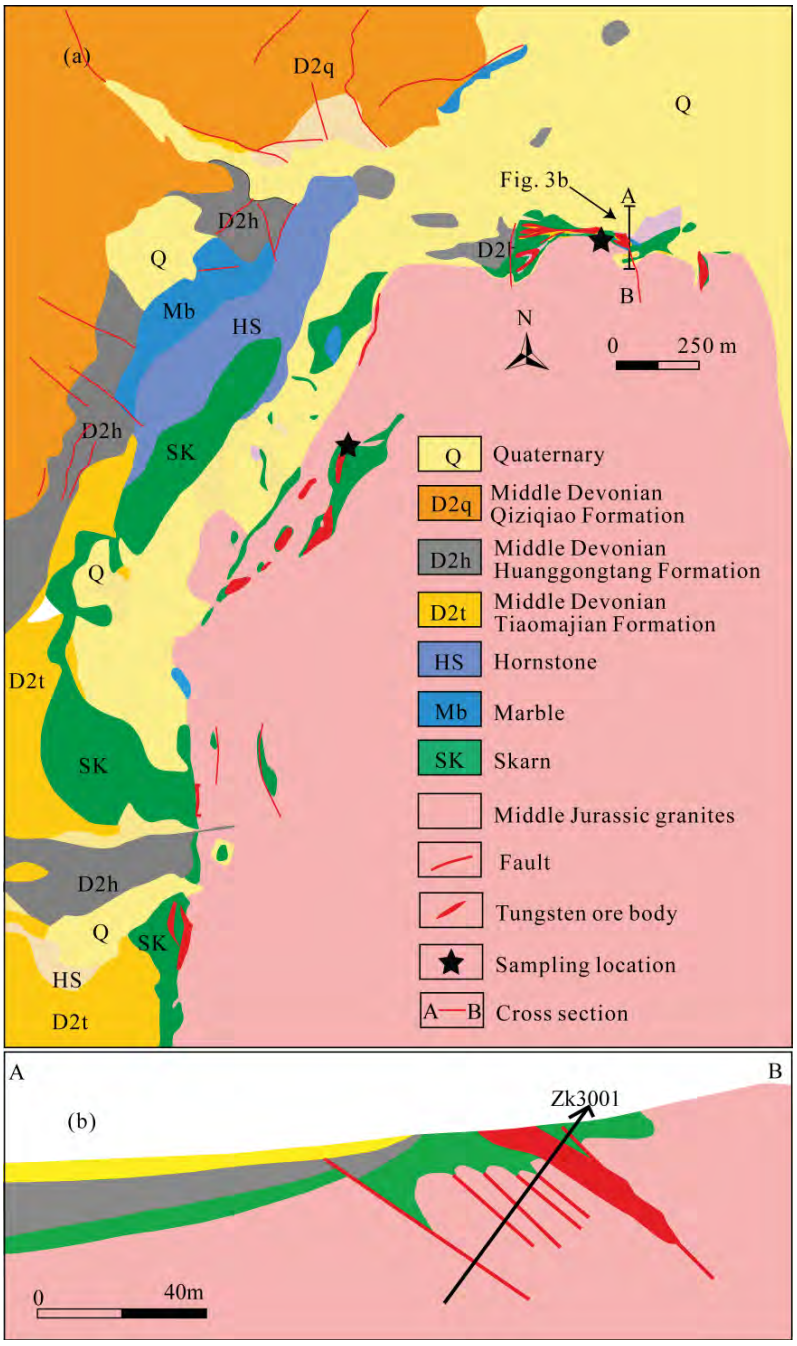

This is the peer-reviewed, final accepted version for American Mineralogist, published by the Mineralogical Society of America.
The published version is subject to change. Cite as Authors (Year) Title. American Mineralogist, in press.
DOI: https://doi.org/10.2138/am-2021-7678. http://www.minsocam.org/

Figure 4

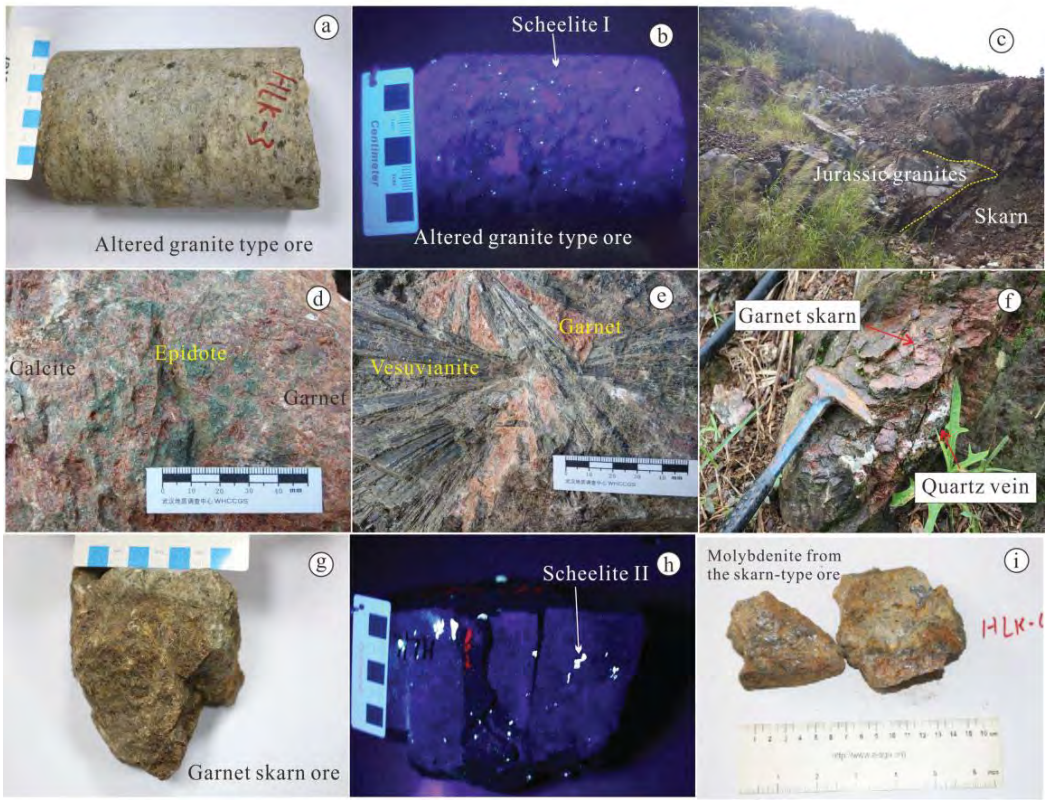

This is the peer-reviewed, final accepted version for American Mineralogist, published by the Mineralogical Society of America.
The published version is subject to change. Cite as Authors (Year) Title. American Mineralogist, in press.
DOI: https://doi.org/10.2138/am-2021-7678. http://www.minsocam.org/

Figure 5

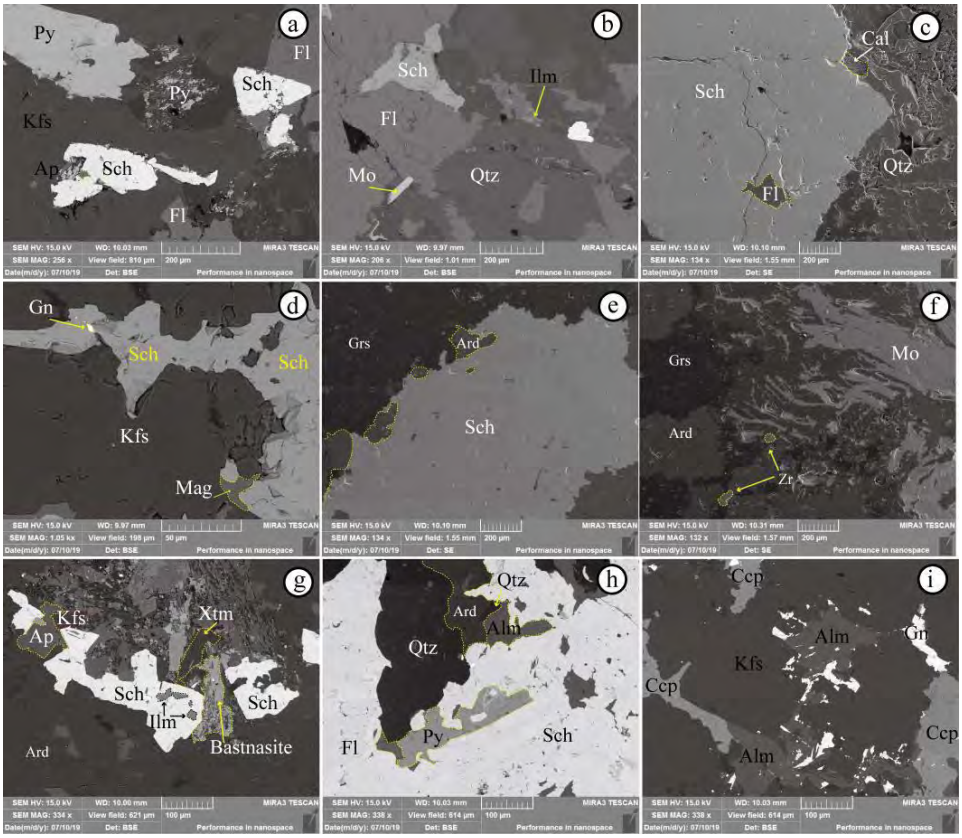

Figure 6

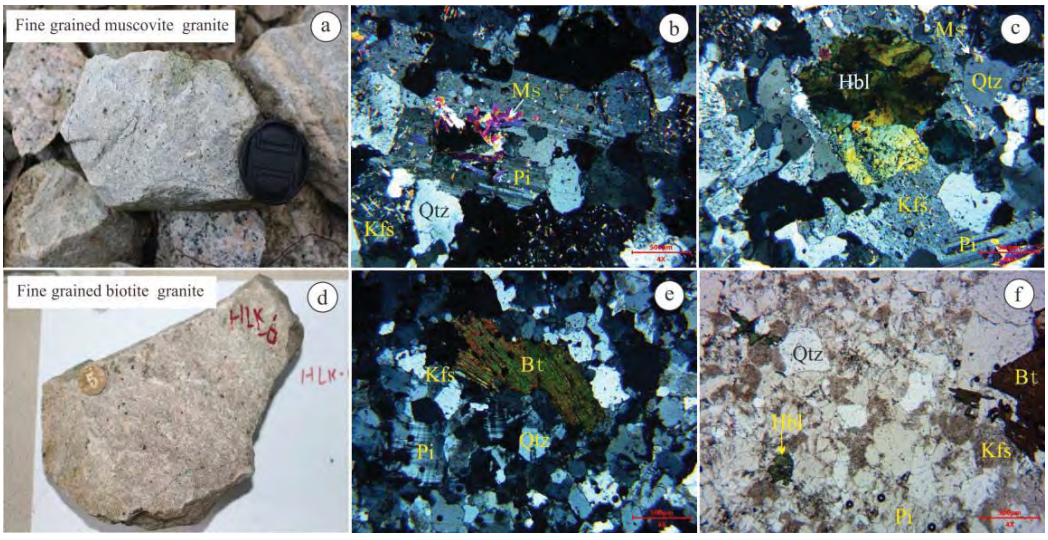

Figure 7

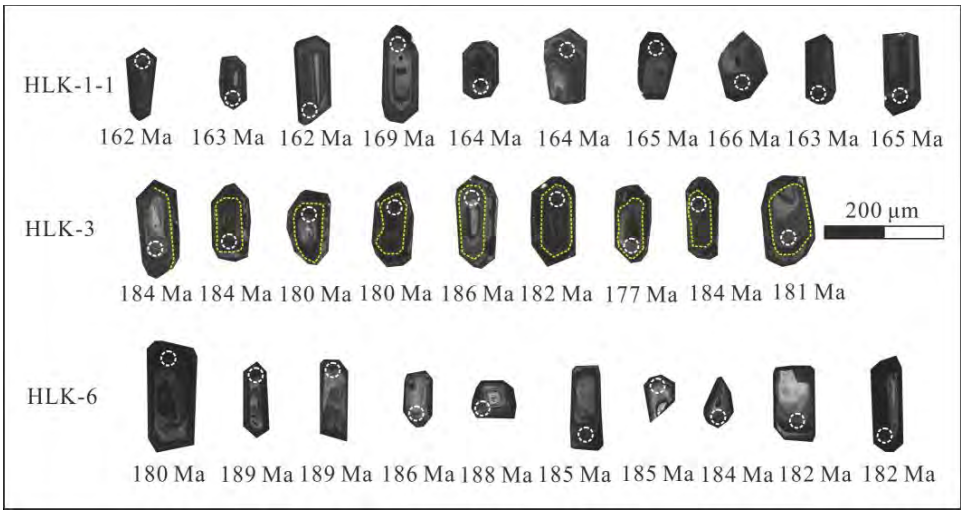

Figure 8

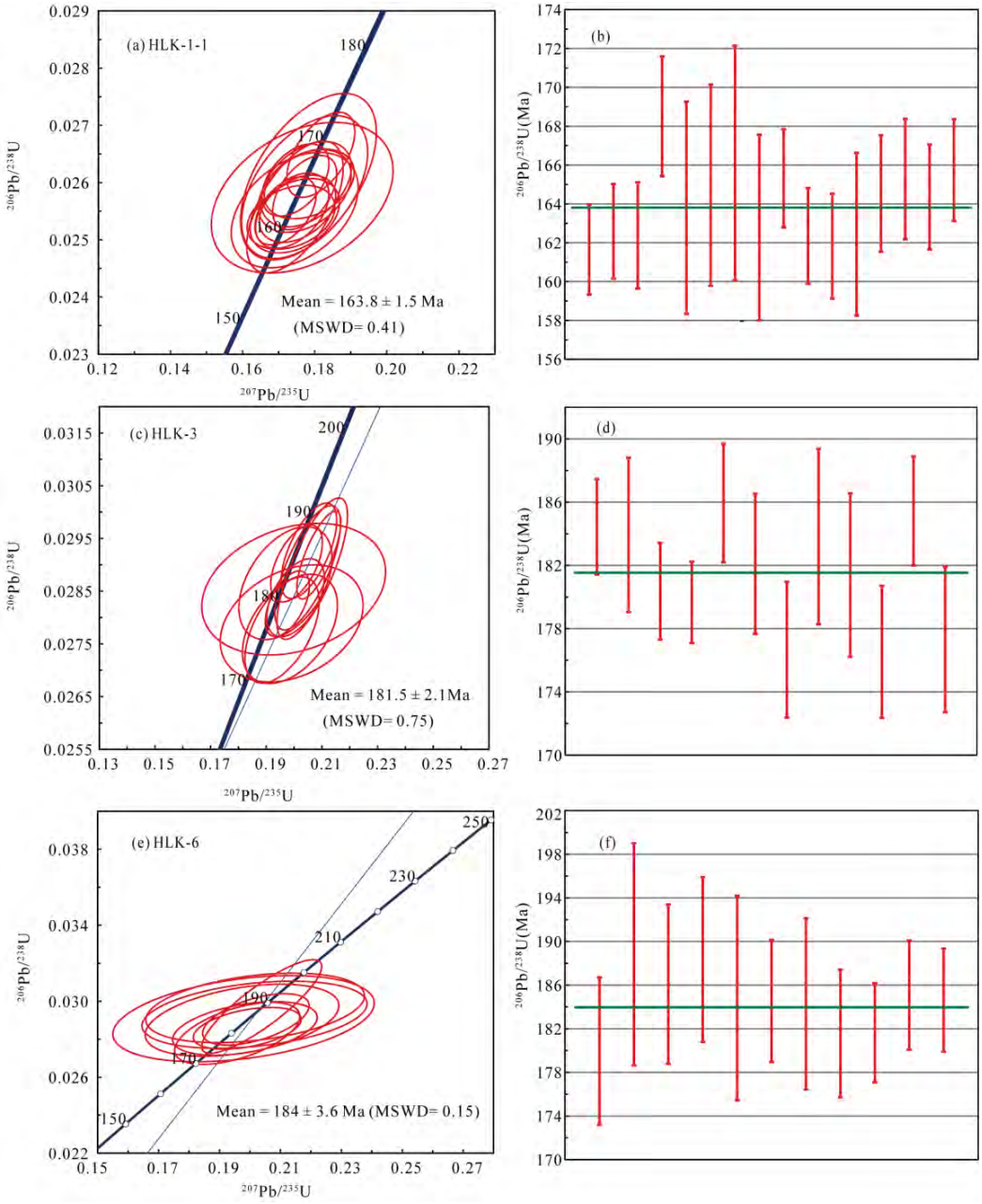

This is the peer-reviewed, final accepted version for American Mineralogist, published by the Mineralogical Society of America.
The published version is subject to change. Cite as Authors (Year) Title. American Mineralogist, in press.
DOI: https://doi.org/10.2138/am-2021-7678. http://www.minsocam.org/

Figure 9

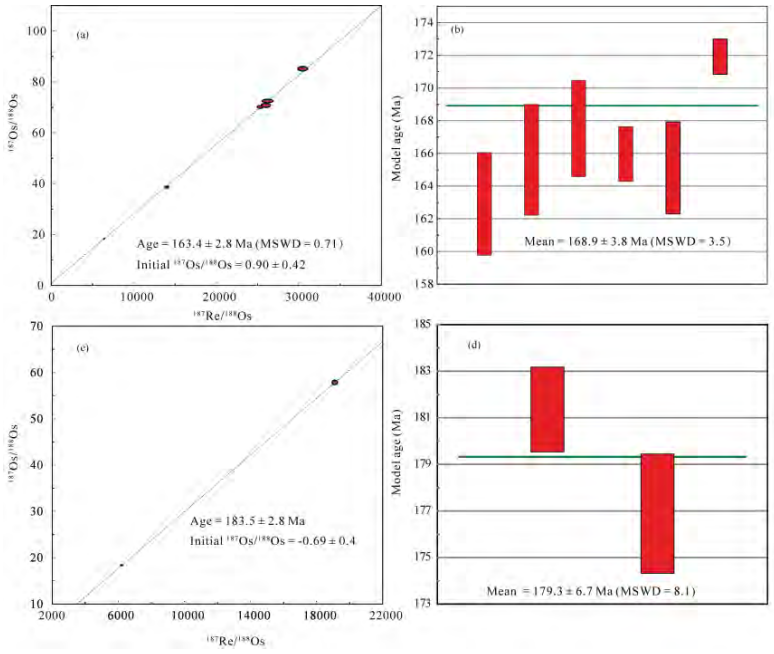

Figure 10

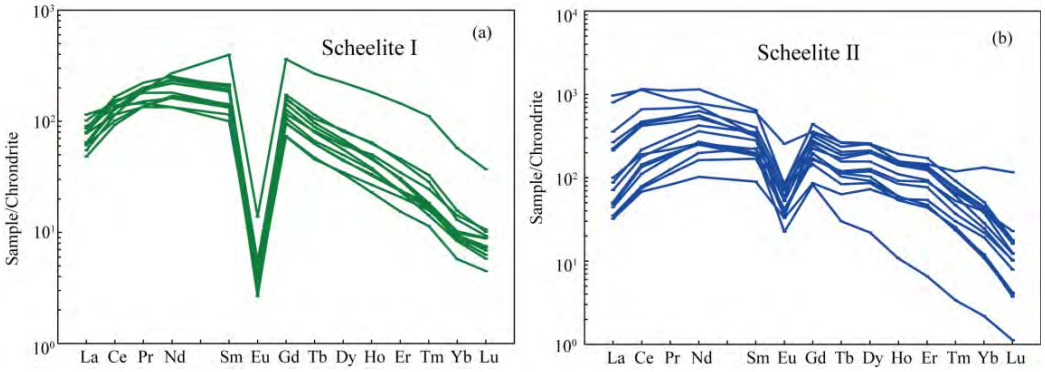

This is the peer-reviewed, final accepted version for American Mineralogist, published by the Mineralogical Society of America.
The published version is subject to change. Cite as Authors (Year) Title. American Mineralogist, in press.
DOI: https://doi.org/10.2138/am-2021-7678. http://www.minsocam.org/

Figure 11

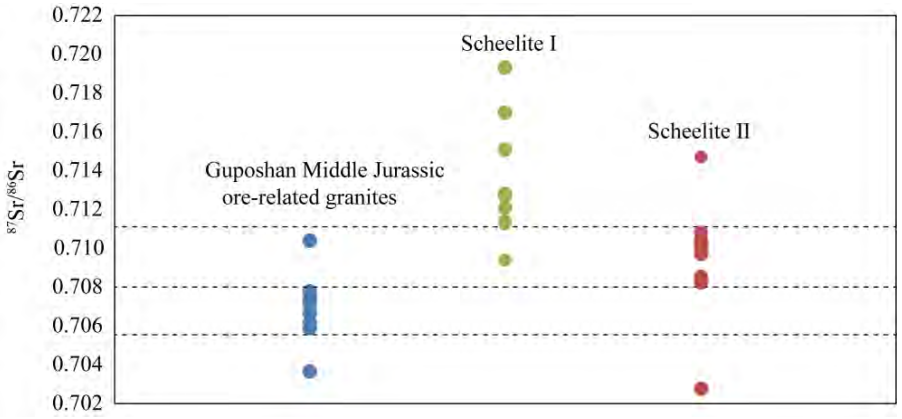

Figure 12